

# Including ash in UKESM1 model simulations of the Raikoke volcanic eruption reveal improved agreement with observations

Alice F. Wells<sup>1</sup>, Andy Jones<sup>2</sup>, Martin Osborne<sup>2</sup>, Lilly Damany-Pearce<sup>1</sup>, Daniel G. Partridge<sup>1</sup> and James M. Haywood<sup>1,2</sup>

5 <sup>1</sup>Faculty of Environment, Science and Economy, Department of Mathematics and Statistics, University of Exeter, Exeter, EX4 4QE, United Kingdom

<sup>2</sup>Met Office, Exeter, EX1 3PB, United Kingdom

*Correspondence to:* Alice F. Wells (afw207@exeter.ac.uk)

**Abstract.** In June 2019 the Raikoke volcano located in the Kuril Islands, northeast of Japan, erupted explosively and emitted  
10 approximately  $1.5\text{Tg} \pm 0.2\text{Tg}$  of  $\text{SO}_2$  and  $0.4 - 1.8\text{Tg}$  of ash into the upper troposphere and lower stratosphere. Volcanic ash is usually neglected in modelling stratospheric climate changes since larger particles have generally been considered to be short-lived in terms of their stratospheric lifetime. However, recent studies have shown that the coagulation of mixed particles with ash and sulfate is necessary to model the evolution of aerosol size distribution more accurately. We perform simulations using a nudged version of the UK Earth System Model (UKESM1) that includes a detailed 2-moment aerosol microphysical  
15 scheme for modelling the oxidation of sulfur dioxide ( $\text{SO}_2$ ) to sulfate aerosol and the detailed evolution of aerosol microphysics in the stratosphere. We compare the model with a wide range of observational data. The current observational network including satellites and surface based lidars and high-altitude sun-photometers means that smaller-scale eruptions such as Raikoke provide unprecedented detail of the evolution of volcanic plumes and processes, but there are significant differences in the evolution of the plume detected using the various satellite retrievals. These differences stem from fundamental  
20 differences in detection methods between e.g. lidar and limb-sounding measurement techniques and the associated differences in detection limits and the geographical areas where robust retrievals are possible. This study highlights that, despite the problems in developing robust and consistent observational constraints, the balance of evidence suggests that including ash in the model emission scheme provides a more accurate simulation of the evolution of the volcanic plume within UKESM1.

## 1 Introduction

25 Throughout history large explosive volcanic eruptions have resulted in periodic perturbations to the climate. Explosive volcanic eruptions frequently emit a combination of gases, including sulfur dioxide ( $\text{SO}_2$ ) and volcanic ash into the UTLS (Upper Troposphere-Lower Stratosphere) where the  $\text{SO}_2$  oxidises resulting in the formation of secondary sulfate aerosols. Sulfate aerosols in the stratosphere have a residence time of several months to a few years (e.g. Robock, 2000; Langmann, 2014; Jones et al., 2017) due to limited wet and dry deposition rates (Kloss et al., 2021). Sulfate aerosols are primarily reflective  
30 and enhance the scattering of shortwave solar radiation, increasing the albedo of the planet and thus exert a cooling effect on

the Earth's climate system (e.g., Robock, 2000; Gordeev, 2014). The extent of their impact upon the climate is dependent on a multitude of parameters, including the magnitude of the emission, location of the volcano, the injection altitude, and the composition of the plume (e.g. Jones et al., 2017).

35 In June 1991 Mount Pinatubo injected an estimated 10-20 Tg of SO<sub>2</sub> into the lower stratosphere (Bluth et al., 1992; Dhomse et al., 2014) causing potentially the largest aerosol perturbation to the stratosphere in the 20<sup>th</sup> century and resulting in average lower tropospheric global temperatures cooling by around 0.5°C across a period of nearly two years (McCormick et al., 1995; Guo et al., 2004). Whilst there has not been another volcanic eruption since Pinatubo to have such a significant impact on the global climate in subsequent years, there have been a series of more moderate eruption. Kasatochi in Alaska erupted in August  
40 2008, injecting an estimated 0.9 – 2.7 Tg of SO<sub>2</sub> (Corradini, et al., 2010; Kravitz et al., 2010; Karagulian et al., 2010). The following year in June 2009, Sarychev Peak on the Kuril Islands was estimated to have injected 1.2 ± 0.2 Tg (Haywood et al., 2010) and in June 2011 Nabro in Eritrea erupted injecting around 1.3 – 1.5 Tg of SO<sub>2</sub> (Clarisse et al., 2012). These eruption estimates for the three volcanic eruptions were later refined using a consistent algorithm; 0.9 Tg, 1.5 Tg and 0.5 Tg loadings were derived above 10km using the Michelson Interferometer for Passive Atmospheric Sounding (MIPAS) on Envisat  
45 (Höpfner et al., 2015). Haywood et al., (2014) estimate that over the period 2008 – 2012 these smaller volcanic eruptions contributed to between -0.02 and -0.03 K of cooling at the Earth's surface.

While these volcanic eruptions injected an order of magnitude less SO<sub>2</sub> into the stratosphere than Pinatubo, monitoring the transport, evolution and dispersion of volcanic plumes allows an assessment of the performance of global climate models in  
50 representing stratospheric sulfate plumes, and allows improvements to be made in key processes. The much-improved observational network compared to that which observed the Pinatubo eruption, which includes satellite observations of both SO<sub>2</sub> (e.g. Cai et al., 2022) and sulfate aerosol (Lee et al., 2009), surface based lidars (e.g. Chouza et al., 2020), high-altitude sun-photometers (e.g. Toledano et al., 2018), and periodic balloon-borne observations (e.g. Jégou et al., 2013) means that observations of these smaller-scale eruptions provide unprecedented detail of the evolution of volcanic plumes and processes.  
55 The validation and improvement of representation of volcanic plumes within global climate models leads to a better understanding of their associated cooling impacts. Such synergy between observations and models also provides a means to assess the uncertainties associated with proposed stratospheric aerosol injection climate intervention strategies that have recently been suggested as a method to ameliorate the worst impacts of climate change (e.g. Lawrence et al., 2018).

60 This study examines the impact of the 2019 eruption of Raikoke. Almost exactly a decade after the eruption of Sarychev Peak (12<sup>th</sup> June 2009, 48.1°N, 153.2°E) on 21<sup>st</sup> June 2019 at 1800 UTC, a neighbouring volcano – Raikoke (48.3°N, 153.2°E) – started to erupt, generating a series of distinct explosive events, and emitting a plume of ash and SO<sub>2</sub> into the stratosphere. During this period, it is estimated that it injected around 1.5 ± 0.2 Tg of SO<sub>2</sub> (Muser et al., 2020; Kloss et al., 2021; De Leeuw et al., 2021) and 0.4 – 1.8 Tg of ash (Bruckert et al., 2022) into the stratosphere signifying the largest volcanic emission of SO<sub>2</sub>

65 since the Nabro eruption in 2011. The resultant volcanic aerosol plume was detected at altitudes ranging between 11 to 20km  
by the TROPOMI instrument (Hedelt et al., 2019; Vaughan et al., 2021) and at similar altitudes by other satellite instruments  
(e.g., Gorkavyi et al., 2021, Kloss et al., 2021), although altitudes as high as 26km have been inferred in isolated lidar  
measurements (e.g. Chouza et al., 2020). These findings indicate that a significant portion of the volcanic plume was injected  
70 the eruption date with an SO<sub>2</sub> e-folding lifetime of approximately 19 days. Previous studies looking at similar volcanic  
eruptions have found SO<sub>2</sub> e-folding times at a similar scale. For example, once the retrieval minimum detection threshold had  
been accounted for, Haywood et al., (2010) determined an e-folding for SO<sub>2</sub> from the Infrared Atmospheric Sounding  
Interferometer (IASI) for the Sarychev Peak eruption of around 20-22 days.

75 Less than a week after the eruption of Raikoke a second volcanic eruption occurred – Ulawun (5.1°S, 151.3°E) – on 26<sup>th</sup> June  
2019 and again on 3<sup>rd</sup> August 2019. It is estimated to have injected around 0.14 Tg SO<sub>2</sub> into the stratosphere during the first  
explosive eruptive phase and a further 0.2 Tg SO<sub>2</sub> during the second phase of the eruption (Kloss et al., 2021).

The Raikoke and Ulawun eruptions were both well observed by a series of satellite instruments and ground-based measurement  
80 stations. Satellite observations include the Ozone Mapping Profiler Suite (OMPS) Nadir Mapper (NM) (Yang, 2017) and Limb  
Profiler (LP) (Taha, 2020) and the Cloud-Aerosol Lidar with Orthogonal Polarization (CALIOP) (Winker et al., 2009) while  
surface observations include those from high altitude AEROSOL ROBOTIC NETWORK sites (AERONET; Holben et al., 1998).  
Although the perturbations to the Earth's radiation budget and near-surface temperature from moderate volcanic eruptions,  
such as Raikoke, are unlikely to be detectable owing to the small signal-noise ratio, these impacts can be estimated from Earth  
85 System models. The Raikoke eruption was the largest volcanic stratospheric injection of SO<sub>2</sub> since the OMPS satellite was  
launched in late 2011 providing an excellent opportunity to assess the skill and the limitations of the UK Earth System Model  
(UKESM1; Sellar et al., 2019) in simulating the evolution of the atmospheric distributions of SO<sub>2</sub> and sulfate aerosol.

Recent studies have drawn attention to the influence of ash on self-lofting and the evolution of the volcanic plume (e.g., Muser  
90 et al., 2020; Kloss et al., 2021). Volcanic ash is usually neglected in the modelling the impact of eruptions on the stratosphere  
and climate since larger particles (radii  $r > 1\mu\text{m}$ ) would be short lived owing to their considerable fall-speed (Niemeier et al.,  
2021, 2009; Stenchikov et al., 2021). However, Zhu et al., 2020 showed that, to produce the evolution of the size distribution  
following the Kelud eruption in 2014, the coagulation of internally mixed ash and sulfate particles is necessary. They also  
found that after this eruption super-micron sized ash particles with an estimated density ( $0.5\text{ g cm}^{-3}$ ) corresponding to pumice  
95 were the main component of the volcanic aerosol layer. This is in contrast to the assumed density ( $\sim 2.3\text{ g cm}^{-3}$ ) of ash within  
current models. Including ash emissions in model simulations has been found to alter the dynamics of sulfate aerosol formation  
(Shallcross et al., 2021; Stenchikov et al., 2021) including prolonging the lifetime of stratospheric aerosol optical depth (sAOD)  
(Kloss et al., 2021). Stenchikov et al. (2021) and Abdelkader et al. (2023) agreed that when modelling the Pinatubo eruption,

including volcanic ash increases the radiative heating during the first week after the eruption and results in the lofting of the  
100 aerosol.

Muser et al. (2020) examined the impacts of aerosol-radiation interactions and aerosol dynamics on volcanic aerosol dispersion. They showed that during the first days after the Raikoke eruption, the absorption of solar radiation caused by the presence of ash had a significant impact on the aerosol dispersion, producing a self-lofting effect on the plume. Over the course  
105 of 4 days after the eruption, the maximum cloud top height rose more than 6km (Muser et al., 2020). Within a few weeks the volcanic plume dispersed across the Northern Hemisphere (NH) and was continually observed months after the eruption. The radiative self-lofting could explain some of the differences between observations and model simulations which did not account for ash in previous studies (Haywood et al., 2010; Kloss et al., 2021) since the self-lofting effect would result in a greater fraction of the plume in the stratosphere and subsequently result in a longer residence time. Stenchikov et al. (2021) also found  
110 in model experiments of the Pinatubo eruption that during the first week after the eruption SO<sub>2</sub> and sulfate plumes in the presence of ash rose 7km above injection. It has been shown that whilst the ash does not provide a direct climate impact and the aerosol optical depth decreases quickly, the impact of the ash on the dynamical lofting of the plume is very important for the mass of the aerosol remaining in the stratosphere (Stenchikov et al., 2021).

115 Several studies have also discussed the influence of self-lofting caused by the presence of soot from intense forest fires (e.g. Fromm et al., 2005; Peterson et al., 2018; Christian et al., 2019; Damany-Pearce, 2022). Of particular note are the studies of Ansmann et al., (2021) and Ohneiser et al., (2021) who used state-of-the-art lidar retrievals mounted on an ice-breaker ship that drifted in the Arctic circle during winter 2020 to infer that biomass burning smoke from intense Siberian wildfires was present in significant quantities in the lower stratosphere, although these results remain contentious (e.g. Boone et al., 2022).  
120 We restrict our study to simulations of the Raikoke eruption including and excluding volcanic ash.

The aim of this study is to assess the modelled volcanic emissions that best represent the observed Raikoke volcanic eruption. We compare observations with a model simulation injecting only SO<sub>2</sub> with a model simulation with both SO<sub>2</sub> and ash. We use these to establish both how well UKESM1 performs in modelling the volcanic plume and to determine if the inclusion of ash  
125 in modelled volcanic emissions leads to a better agreement with observations. In Sect. 2 we introduce the observational data sets used and the differences in retrieval techniques. Furthermore, we provide a description of UKESM1, and the simulation set up in Sect. 3. In Sect. 4 we present the results and discussion before conclusions are drawn in Sect. 5.

## 2. Observational data and quality assurance

### 2.1 CALIPSO

130 The Cloud-Aerosol Lidar and Infrared Pathfinder Satellite Observation (CALIPSO) satellite (Winker et al., 2009) combines  
an active lidar instrument with passive infrared and visible imagers to analyse the vertical structure and properties of thin cloud  
and aerosols. The Cloud-Aerosol Lidar with Orthogonal Polarization (CALIOP) instrument is a dual-wavelength (532nm and  
1064nm) polarization-sensitive lidar which provides high-resolution vertical profiles of aerosols and clouds. The aerosol  
profile products are reported at a uniform spatial resolution of 5km horizontally. The vertical resolution of the data varies as a  
135 function of altitude, with 60m vertical resolution in the troposphere and 180m vertical resolution in the stratosphere.

This study uses quality-assured (QA) daily averaged vertical profiles of aerosol extinction ( $\text{km}^{-1}$ ) at 532nm from the Version  
4.20 CALIOP 5km Level 2 Cloud and Aerosol Profile data product. Aerosol extinction coefficients are reported for each bin  
in which aerosol particulates were detected, those in which no aerosols were detected contain fill values (-9999) and those in  
140 which the extinction retrieval failed were assigned a fill value of -333. These were mapped to a  $1^\circ \times 1^\circ$  latitude/longitude  
spatial grid whilst maintaining the original vertical profile. Quality control procedures were applied to the data in a similar  
fashion to those implemented in Campbell et al. (2012) which includes quality assurance on the stability of the retrievals and  
accounts for missing data when retrieval stability fails. The stratospheric aerosol optical depth is calculated by integrating over  
altitudes above the observed tropopause.

145 Active lidar retrievals, such as those obtained by CALIOP, are susceptible to solar background contamination which results in  
poorer performance in day-time conditions resulting in different minimum detection thresholds. It is estimated that the night-  
time threshold is  $0.012 \text{ km}^{-1}$  and the day-time thresholds is  $0.067 \text{ km}^{-1}$  (Toth et. al., 2018). The day-time detection threshold  
results in a column integrated underestimate of the AOD, and it has been found that it is unable to detect around 50% of aerosol  
150 profiles when the AOD is less than 0.1 (Toth et. al., 2018). For this reason, this study only uses the night-time retrievals to  
create the daily average extinction values to avoid an underestimated daily average. However, utilising only the night-time  
profiles leads to large areas of missing data, specifically at high latitudes during the Northern Hemisphere summer where areas  
experience 24 hours of sunlight. At most northern latitudes ( $60^\circ\text{N} - 90^\circ\text{N}$ ) the CALIOP night-time profiles miss the initial  
peak in aerosol between 30 and 100 days after the eruption. Whilst the maximum night-time sAOD is approximately 65%  
155 greater than the peak daytime sAOD, evaluating only the night-time profiles could influence the timing of the sAOD peak.  
This is discussed further in Sect. 4.

### 2.2 OMPS

The Suomi National Polar-orbiting Partnership (NPP) is a weather satellite which was launched in 2011 with five imaging  
systems, including the Ozone Mapping and Profiler Suite (OMPS), a series of instruments comprised of back-scattered

160 ultraviolet radiation sensors. These sensors measure and monitor atmospheric trace gases, aerosols, surface reflectance and cloud-top pressure. There is global spatial coverage providing a good opportunity to evaluate the plume at high latitudes. Retrieved profiles have a vertical resolution of approximately 1.8km, with profiles being measured from the ground to about 80km (Taha et. al., 2021).

165 **2.2.1: OMPS-NM:** The OMPS Nadir Mapper (NM) measures backscattered UV radiance spectra between 300-380nm and whilst it is primarily designed to measure global total ozone, the SO<sub>2</sub> vertical column amount can be derived from the hyperspectral measurements of the OMPS-NM instrument. This study utilises the SO<sub>2</sub> Level 2 orbital products to assess the distribution of SO<sub>2</sub> after the eruption. A QA scheme is applied to daily profiles of total column SO<sub>2</sub> data, retrieved with a prescribed lower stratospheric profile centred at 16km above the surface. The screening includes discarding pixels when the  
170 solar zenith angle is greater than approximately 88° or viewing zenith angle is greater than approximately 70° (Yang, 2017).

**2.2.2: OMPS-LP:** In addition to the CALIOP aerosol extinction data, we utilise retrievals of the vertical aerosol extinction coefficient (km<sup>-1</sup>) from the OMPS Limb Profiler (LP). The OMPS-LP is a passive sensor which looks back along the orbit track at the Earth's limb and records atmospheric spectra which are used to retrieve aerosol extinction coefficient profiles from  
175 the lower stratosphere (10 – 15km) to the upper stratosphere (55km). Aerosol extinction measurements are provided at wavelengths ranging between 510 – 997nm at 1km altitude intervals between the surface and 40.5km. This study utilises the V2.0 data measured at 869nm, which have been found to be the best OMPS-retrieved wavelength relative to SAGE III (Taha et al., 2021). Relative to V1.5 data, an improved cloud screening criterion is used in V2.0, which does not remove fresh volcanic plumes and allows us to use the filtered Retrieved Extinction Coefficient data product which removes the influence  
180 of polar stratospheric clouds (Taha et al., 2021). As with the CALIOP data, quality control procedures are applied to the OMPS-LP data. These include removing values where the cumulative residual error exceeds a threshold value, when the single scattering viewing angle exceeds 145° and where the derived aerosol scattering index is less than 0.01 (Johnson et al., 2020).

Due to the viewing geometry and sensitivity of the instrument, OMPS-LP can detect aerosol extinction coefficient values down  
185 to a minimum value of  $1 \times 10^{-5} \text{ km}^{-1}$  (Johnson et al., 2020), which is far more sensitive than CALIOP (Section 2.1.1). However, OMPS-LP experiences loss of sensitivity of short wavelength radiances to aerosols, caused by Rayleigh scattering and aerosol attenuation of the limb scattered radiation, which is most pronounced below ~17km and especially in the southern hemisphere (Johnson et al., 2020). The retrieval issues described here, particularly the altitude sensitivity, have a significant impact on our study since it was estimated that the initial plume reached altitudes of between 11 and 20km (Vaughan et al., 2021; Osborne  
190 et al., 2022), therefore we utilise the 869nm wavelength data and scale it to 532nm to compare to CALIOP. However, once the self-lofting of the plume occurs and it is dispersed over the northern hemisphere it is expected that the increased sAOD becomes more readily detectable by OMPS-LP (Hirsch and Koren, 2021), while it becomes less detectable or undetectable by CALIOP due to CALIOP's significantly higher minimum detection threshold. This is examined in more detail in Sect. 4.

## 2.3 AERONET

195 AERONET provides whole atmosphere AOD observations at a series of sites distributed across the globe providing a good  
global coverage of ground-based remote sensing data. One of these sites, the Mauna Loa Observatory (MLO), located at 3397m  
above sea level in Hawaii, provides an excellent opportunity to monitor stratospheric events. The measurement site is generally  
removed from the influence of pollution sources and is located at an altitude higher than most tropospheric aerosols. This  
provides an opportunity to retrieve ground-based observations of the stratosphere using sun-photometry with minimal  
200 tropospheric influences. MLO has been monitoring the stratospheric aerosol layer with lidars since 1975 (Barnes and Hofmann,  
1997) providing a long-term historical record and previous studies have demonstrated that aerosol from the Raikoke plume  
was readily detectable (Chouza et al., 2020). Rather than lidars, this study uses daily Level 2 AOD AERONET retrievals  
measured at 500nm which are automatically cloud-cleared and quality assured.

## 3. Model simulations

### 205 3.1 UKESM1

UKESM1 is the latest UK Earth system model, described by Sellar et al. (2019). UKESM1 consists of the HadGEM3 coupled  
physical climate model with additional interactive components including modelling key biogeochemical processes (Yool et  
al., 2013), tropospheric and stratospheric chemistry (Archibald et al., 2020), aerosols (Mann et al., 2010) and sea-ice (Ridley  
et al., 2018). The atmosphere has a horizontal resolution of 1.25° latitude by 1.875° longitude with 85 vertical levels and a  
210 model top at around 85km (Storkey et al., 2018). The StratTrop chemical mechanism used in UKESM1 is described by  
Archibald et al., (2019). This merged stratospheric and tropospheric scheme simulates interactive chemistry from the surface  
to the top of the model, including oxidation reactions responsible for sulfate aerosol production (Sellar et al., 2019).

Atmospheric composition in UKESM1 is simulated by the UK Chemistry and Aerosols (UKCA) sub-model. One of the main  
215 components of UKCA is the GLOMAP-mode modal aerosol scheme described in Mann et al., (2010) and Mann et al., (2012).  
GLOMAP-mode is a two-moment aerosol microphysics scheme which simulates speciated aerosol mass and number across  
five lognormal size modes, 4 soluble modes (nucleation, Aitken, accumulation, and coarse modes) and one insoluble Aitken  
mode. The prognostic aerosol species represented are sulfate, black carbon, organic carbon, and sea salt, with species within  
each mode treated as an internal mixture. The size ranges of covered by each mode are shown in Table 1.

220

Aerosol mode	Radii (nm)	$\sigma_g$
Nucleation sol.	0 – 5	1.59
Aitken sol.	5 – 50	1.59

Accumulation sol.	50 – 250	1.40
Coarse sol.	250 – 5000	2.00
Aitken insol.	5 – 50	1.59

---

**Table 1:** The aerosol size distribution in GLOMAP-mode including the aerosol modes represented, the range of radii that these include and their geometric standard deviation.

225 This configuration for UKESM1 and UKCA has been used in many studies to model the evolution of sulfur dioxide into sulfate  
aerosol, most recently by Visioni et al. (2023) and Bednarz et al (2023), who examined the evolution and climate impacts of  
the sulfur dioxide and sulfate plume under continuous stratospheric injection three different models. In terms of the distribution  
and sulfate aerosol optical depth, the resultant plume from UKESM1 when injecting at the most northerly latitude in that study  
(30°N) was broadly consistent with that from both CESM2 and GISS models, lending confidence to the ability of UKESM1  
230 to accurately model mid-high latitude stratospheric injections.

In addition to the UKCA aerosol components, mineral dust is included as an externally mixed aerosol via the CLASSIC  
(Coupled Large-scale Aerosol Simulator for Studies In Climate) six-bin scheme detailed in Woodward (2011), which  
represents mineral dust with diameters ranging from approximately 0.06 to 60µm. This scheme is modified to provide a suitable  
235 proxy for volcanic ash as detailed in section 3.2.

### 3.2 Simulations and reference wavelengths for model/observation intercomparisons

Simulations of the Raikoke and Ulawun eruptions were performed by nudging horizontal winds towards ERA5 reanalysis data  
to produce relevant meteorological conditions for the respective period using the atmosphere-only configuration of UKESM1.  
240 Nudged simulations were performed without any explosive volcanic emissions as a control (CNTL), SO<sub>2</sub> emissions only  
(SO<sub>2</sub>only) and with SO<sub>2</sub> and ash emissions (SO<sub>2</sub>+ash). The Raikoke eruption was initiated for the 24-hour period starting at  
00:00 UTC on 21<sup>st</sup> June 2019, with a constant emission rate. Emissions were injected into a single column within the model  
framework at two injection altitudes, a lower “tropospheric” injection at 10km and an upper “stratospheric” injection at 13-  
15km where the emissions were distributed equally across the altitude range. A total of 1.5 Tg SO<sub>2</sub> (Kloss et al., 2021) was  
245 injected and, for the SO<sub>2</sub>+ash scenario, 1.1 Tg of ash (Muser et al., 2020) was also injected at the same altitudes as SO<sub>2</sub>.  
Injection altitudes and masses of SO<sub>2</sub> and ash are consistent with observations and those found in the literature (Muser et al.,  
2020; Kloss et al., 2021; De Leeuw et al., 2021). The emission profile was weighted so that 80% was emitted into the  
stratosphere and the remaining 20% into the troposphere, based on observations of the SO<sub>2</sub> vertical profile (De Leeuw et al.,  
2021; Osborne et al., 2022).



250

Emissions of ash are implemented by adapting the Woodward (2011) bin scheme for mineral dust as a suitable proxy. The justification for doing this stems from the fact that the refractive indices and size distributions are similar (e.g. Millington et al., 2012; Johnson et al., 2012; Osborne et al., 2022), although it is recognised that substantial inter-eruption and inter-eruption-phase variability in volcanic ash refractive indices occurs (e.g. Millington et al., 2012; Turnbull et al., 2012). The ash is moderately absorbing with a refractive index of  $1.52 + 0.0015i$ , based on the mineral dust from Balkanski et al., (2007) with the medium level of hematite (1.5%). Volcanic ash size distributions were based on observations of the Eyjafjallajökull eruption presented in Johnson et al. (2012) fitted by lognormal distributions (Table 5 of Johnson et al., 2012). The lognormal parameters for the overall mean aerosol size distribution include a volume geometric mean diameter of 3.8 and standard deviation of 1.85. Transport and deposition of dust is as described in detail in Woodward (2001) with improvements to the emission scheme and refractive index data described in Woodward (2022). In the current configuration mineral dust aerosol is simulated independently of other aerosol species using the CLASSIC dust scheme (Bellouin et al., 2011). Mineral dust can therefore be considered externally mixed with the GLOMAP aerosols.

For both SO<sub>2</sub>only and SO<sub>2</sub>+ash simulations, the Ulawun eruptions are simulated by UKESM1 with an SO<sub>2</sub> only injection (no ash emissions) and are initiated on 26<sup>th</sup> June and 3<sup>rd</sup> August 2019. Injection altitudes for Ulawun were 13-17km (26<sup>th</sup> June) and 14-17km (3<sup>rd</sup> August) using 0.14 Tg and 0.30 Tg SO<sub>2</sub> respectively (Kloss et al., 2021).

To facilitate the intercomparison of the observations and the model simulations all datasets were scaled to 532nm. Mie scattering calculations were performed using the Mie scattering code within SOCRATES (Suite Of Community Radiative Transfer codes based on Edwards and Slingo; Edwards and Slingo, 1996) to generate the single scattering properties of volcanic aerosol at a range of specified wavelengths. Note that both the Mie scattering code and SOCRATES are used in the radiative transfer code within UKESM1. The size distribution of the volcanic aerosol used here was based upon the bimodal lognormal size distribution for a moderate loading volcanic eruption (SPARC, 2006). Specific extinction coefficients were calculated to allow all observational and model data to be scaled to one consistent wavelength: 532nm.

275

#### 4. Results

In analysing the results, we examine the injection of the SO<sub>2</sub> and ash through to the gas phase oxidation of the SO<sub>2</sub> to sulfate aerosol and the ultimate deposition of the aerosol until the stratospheric perturbation is no longer detectable. Different aspects are investigated including the geographic distribution and temporal evolution of the SO<sub>2</sub> and sulfate aerosol and the latitudinal distribution and vertical profile of the sulfate aerosol.

280

## 4.1 Observed and modelled SO<sub>2</sub> including and excluding volcanic ash

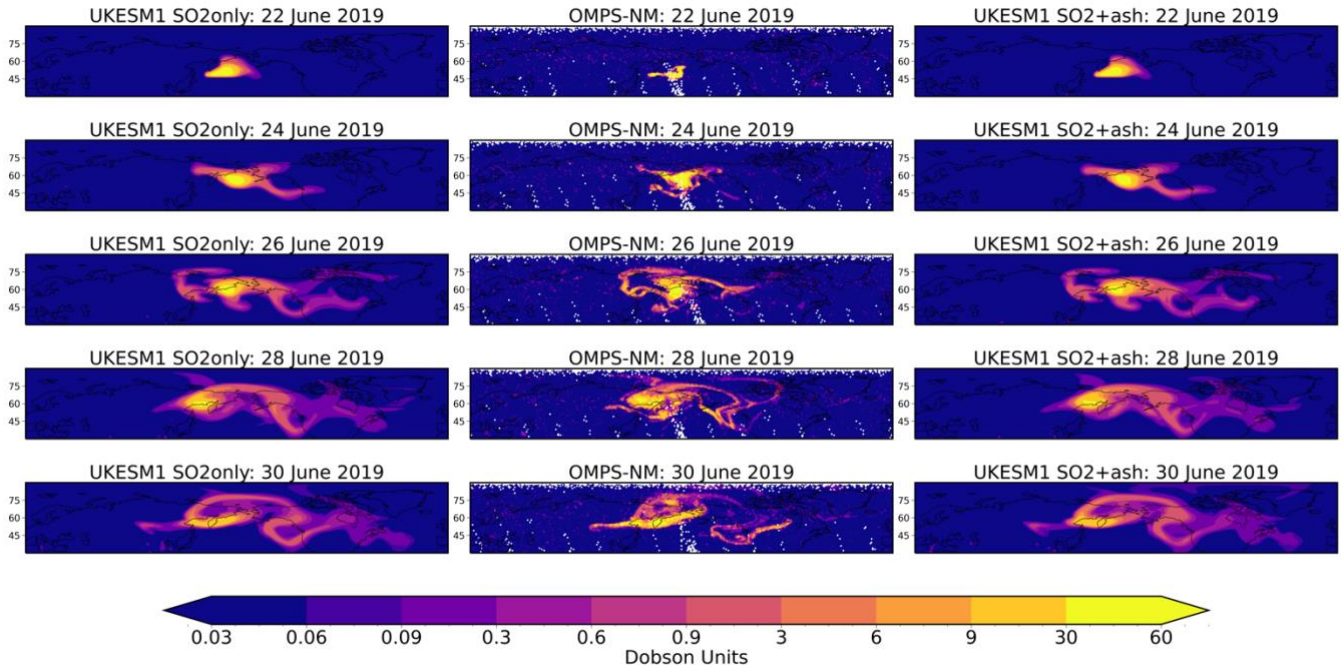


**Figure 1:** Geographic evolution of column integrated SO<sub>2</sub> plume in Dobson Units (DU) derived from OMPS-NM lower stratospheric profile (centre) UKESM1 SO<sub>2</sub>only (left) and SO<sub>2</sub>+ash (right) for the period 22–30<sup>th</sup> June 2019. We remove the long-term background SO<sub>2</sub> burden derived from OMPS-NM for the years 2013–2018 from those for 2019 to provide a stratospheric perturbation for the observations. Similarly, we remove the impacts of background stratospheric aerosol from the model simulations by subtracting the stratospheric sulfate burdens from the CNTL simulation from those for SO<sub>2</sub>only and SO<sub>2</sub>+ash. The OMPS-LP background and CNTL SO<sub>2</sub> burden are shown in Fig. S1.

Figure 1 shows the evolution of the SO<sub>2</sub> cloud from 22<sup>nd</sup> June through to the 30<sup>th</sup> June 2019. The middle column shows the OMPS-NM observations, with the UKESM1 SO<sub>2</sub>only and SO<sub>2</sub>+ash simulations on the left and the right respectively. We see that the position and timing of the plume is relatively well modelled throughout this period in both simulations. There is little difference in the spatial pattern of the SO<sub>2</sub> plume in both simulations, making it difficult to determine based upon SO<sub>2</sub> alone which simulation best represents the observations. Qualitatively, the spatial pattern of the plume is better represented in both the model simulations from 26<sup>th</sup> June onwards, with both the easterly and westerly parts of the plume well modelled. The largest difference between the observations and the model simulations is seen on 22<sup>nd</sup> June where the model is initially much more diffuse. This is due to the eruption taking place at 18:00 UTC 21<sup>st</sup> June and it was inherently explosive and sporadic in nature compared to the smooth injection rates that are assumed in the model. This could explain why the modelled plume does not represent the observations as well during the first two days after the eruption. Similar conclusions have been found in a

300 recent modelling study that use the CALIOP lidar to assess the fidelity of an operational dispersion model in determining the evolution of a large pyro-cumulonimbus event (Osborne et al., 2022; their Figure 7). Since the model does a reasonable job at representing the shape and distribution of the plume after a few days, and our objectives are to assess the general model performance over a period of many months, we retain our simplified emission period and assumed vertical profile. Higher resolution modelling assessments using the Met Office Numerical Atmospheric-dispersion Modelling Environment (NAME),  
305 that are more appropriate for operational monitoring of volcanic plumes for the first few weeks after the eruption for the purposes of aviation safety are available in de Leeuw et al., (2021) and Osborne et al., (2022).

In the first few days after the eruption the SO<sub>2</sub> plume becomes trapped within a cyclonic circulation across Eastern Russia and Alaska (e.g. Osborne et al., 2022). We can observe this feature in both the observations and the model simulations. However,  
310 as observed in other similar studies of other volcanic eruptions (e.g., Haywood et al., 2010) the model SO<sub>2</sub> plume becomes more diffuse than observations over time. We can see that as the plume evolves, despite the model capturing the general position, the model overestimates the tail crossing North America and underestimates the magnitude of the plume over Russia. This can also be due to the instrumental detection limits, where the plume has become so diffuse it becomes undetectable. We also notice that the model is generally more diffuse than the observations, which has been observed with other numerical  
315 transport schemes (e.g. de Leeuw et al., 2021), which could contribute to the differences seen in the modelled and observed tails.

To provide a more quantitative analysis of the geographic evolution we employ a dichotomous forecast style analysis. A contingency table is a simple way to identify the frequency of “yes, an event will happen” and “no, the event will not happen”  
320 forecasts and occurrences. For this analysis we treat the model simulation as the forecast and the observations as the occurrence for each grid box on each day. There are four combinations of simulations and observations, “*hits*” – the model simulates the observations correctly, “*model > observations*” – the model overestimates the observations, “*observations > model*” – the model underestimates the observations and “*correct negative*” – both the observations and the model are below a given threshold, 0.3 Dobson Units (DU). In developing the contingency table we consider estimates of error such as timing errors in  
325 synoptic meteorological features that frequently occur in weather forecasting and the fact that the model and observations are not perfectly collocated in time. We therefore assume that the observations are uncertain by a factor of two and use these as the upper and lower bounds. However, we recognise that much more detailed and comprehensive approaches to forecast verification have been developed (e.g. Casati et al., 2008).

330 Figure 2 presents this analysis for the first 10 days after the eruption. Both simulations show a similar distribution, so we focus on SO<sub>2</sub> only here. It is clear that “*model > observations*” dominates, with a large tail over North America, as seen in Figure 1. However there are some regions where the model is underestimating the observations which may not have been identified by eye in Figure 1. Over the 20 days after the eruption, approximately the time for the oxidation of SO<sub>2</sub> to sulfate aerosol, both

model simulations overestimate the observed plume 52% of the time. We also note that between 15 – 17% of the plume is  
 335 correctly modelled within the bounds of the observations for both simulations, with SO<sub>2</sub>+ash underestimating the observations  
 3% more than SO<sub>2</sub>only (Table 2).

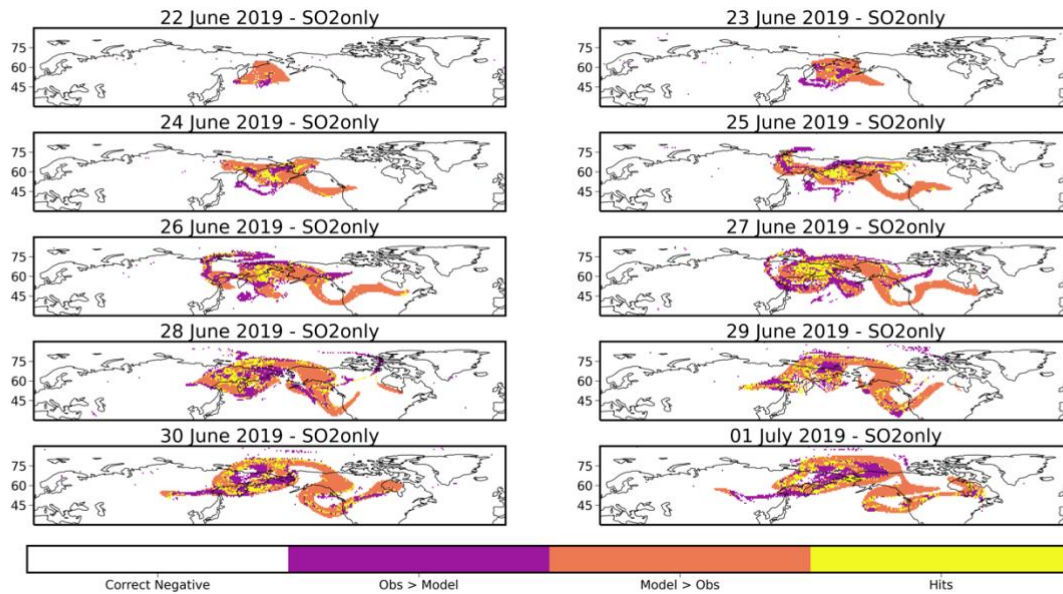


**Figure 2:** Contingency analysis of SO<sub>2</sub> plume between OMPS-NM lower stratospheric profile and UKESM1 SO<sub>2</sub>only for the  
 period 22<sup>nd</sup> June–1<sup>st</sup> July 2019. “Correct Negative” occurs at the point where both the model and observation are below 0.3  
 340 DU. “Hits” occur at the point where the modelled column SO<sub>2</sub> burden is within a factor of two of the observations at that point  
 to allow for timing errors. “Obs > Model” and “Model > Obs” occur when the modelled column SO<sub>2</sub> burden is above or below  
 the factor of two limit.

	“Hits”	“Observations > Model”	“Model > Observations”
SO <sub>2</sub> only	17%	31%	52%
SO <sub>2</sub> +ash	15%	34%	51%

**Table 2:** Contingency analysis of SO<sub>2</sub> plume between OMPS-NM lower stratospheric profile and UKESM1 SO<sub>2</sub>only and  
 345 SO<sub>2</sub>+ash for the 20 days following the eruption on 21<sup>st</sup> June 2019. “Hits” occur at the point where the modelled column SO<sub>2</sub>  
 burden is within a factor of two of the observations at that point to allow for timing errors. “Obs > Model” and “Model > Obs”  
 occur when the modelled column SO<sub>2</sub> burden is above or below the factor of two limit.

In Figure 1 we can see that the SO<sub>2</sub> plume travels longitudinally and moves towards more northern latitudes, as we would expect from the stratospheric Brewer-Dobson circulation (e.g. Haynes, 2005), and as evidenced from the previous eruption of Sarychev Peak (Haywood et al., 2009; Jégou et al., 2013). Due to this poleward transport, it is unlikely that the Raikoke SO<sub>2</sub> plume would travel south of 30°N, particularly in the first few months after the eruption. Hence, to avoid any influence from the Ulawun eruption we take the area weighted average from 30 – 90°N (discussed further in Sect. 4.3) to determine the temporal evolution of SO<sub>2</sub> and calculate an *e*-folding time. Figure 3 shows the daily column burden of observed and modelled SO<sub>2</sub> after the eruption. The spike seen at approximately day 60 is an artifact from the long-term background SO<sub>2</sub> burden. The observations show a peak column burden of 0.76 DU and have an *e*-folding time of 20 days. Model simulations had similar *e*-folding times of 19 and 21 days for SO<sub>2</sub>only and SO<sub>2</sub>+ash respectively. This suggests that the oxidation processes are well represented in the UKESM1 model and are very similar to those determined for the Sarychev Peak eruption for the fore-running HadGEM-2 climate model (Haywood et al., 2010). However, in both SO<sub>2</sub>only and SO<sub>2</sub>+ash model simulations the peak SO<sub>2</sub> column burden is only 0.44 DU, considerably less than that observed by OMPS-NM. The notable difference between the observations and the model is unexpected given that the magnitude of SO<sub>2</sub> injected was based on observations (Muser et al., 2020; Kloss et al., 2021; De Leeuw et al., 2021). However, if the amount of SO<sub>2</sub> injected into the model simulations were to be increased it would lead to a significant overestimate of sulfate aerosol and sAOD (see later sections). For this reason we do not change the amount of SO<sub>2</sub> injected. We do note that the 1.5 Tg of SO<sub>2</sub> that we chose to inject into UKESM1 is based upon measurements from TROPOMI and HIMAWARI data and therefore may not exactly correlate with the OMPS-NM data.

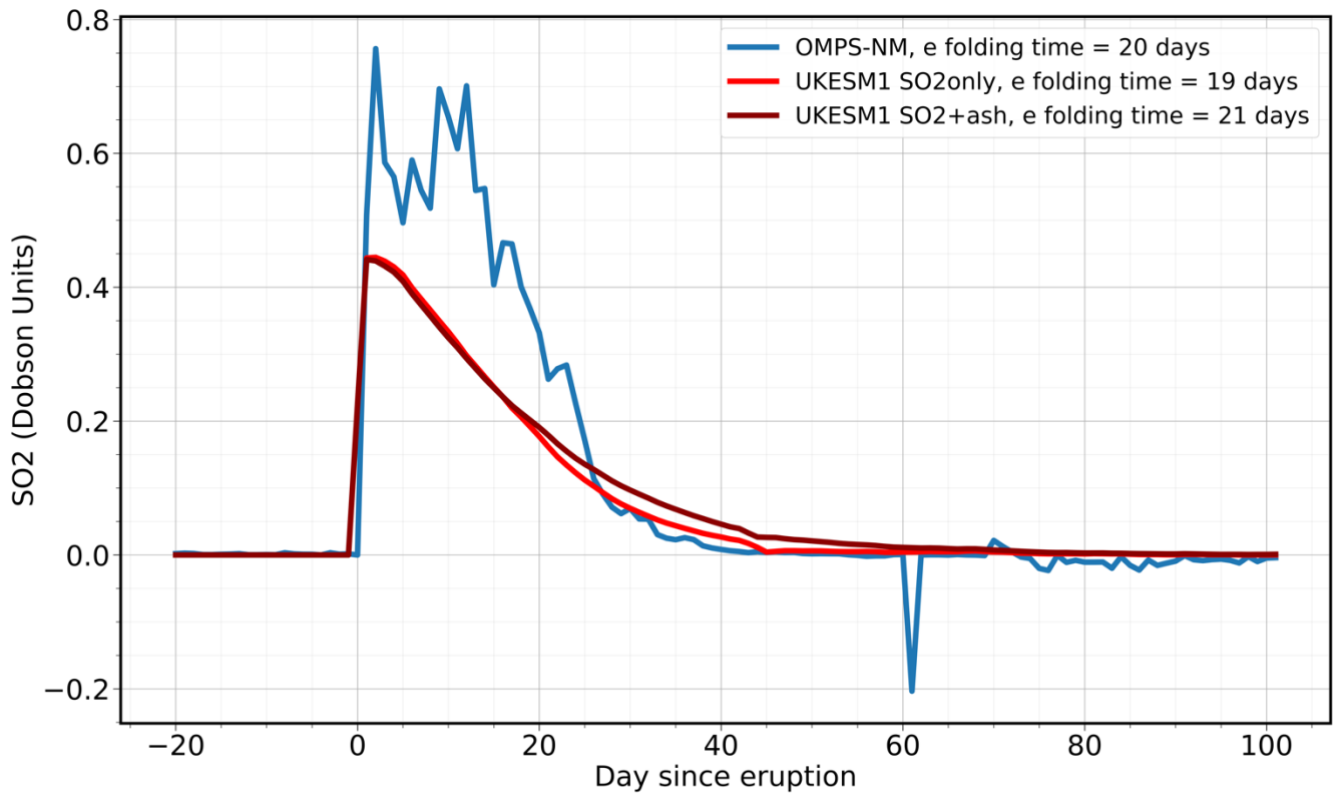


**Figure 3:** Daily perturbation of  $\text{SO}_2$  in Dobson Units (DU) derived from OMPS-NM lower stratospheric profile (blue), UKESM1  $\text{SO}_2$ only (red)  $\text{SO}_2$ +ash (dark red). Data averaged across latitudes  $30\text{--}90^\circ$  N, weighted by the cosine of the corresponding latitude to ensure data is area weighted. We remove the long-term background  $\text{SO}_2$  burden derived from OMPS-NM for the years 2013–2018 from those for 2019 to provide a stratospheric perturbation for the observations. Similarly, we remove the impacts of background stratospheric aerosol from the model simulations by subtracting the stratospheric sulfate burdens from the CNTL simulation from those for  $\text{SO}_2$ only and  $\text{SO}_2$ +ash.

#### 4.2 Distribution of sulfate aerosol

To investigate the distribution and evolution of the sulfate plume we utilise the CALIOP and OMPS-LP retrieved aerosol extinction integrated above the tropopause to find the perturbed sAOD. We firstly investigate the temporal evolution of the zonal mean sAOD by performing similar analysis to previous studies (e.g., Kravitz et al., 2010; Haywood et al., 2010; Kloss et al., 2021). We compare the evolution of the OMPS-LP and CALIOP retrievals against the UKESM1  $\text{SO}_2$ only and  $\text{SO}_2$ +ash scenarios, shown in Figure 4. Due to the differences in satellite retrievals discussed in Section 2, there are seasonal gaps in the data from as far south as  $\sim 55^\circ\text{N}$  in CALIOP night-time retrievals, due to polar summer and  $\sim 65^\circ\text{N}$  in OMPS-LP due to the

lack of daylight hours in NH winter. Additionally, the observations have different minimum retrieval limits ( $0.012 \text{ km}^{-1}$  for CALIOP,  $1 \times 10^{-5} \text{ km}^{-1}$  for OMPS-LP) so to ensure better comparisons we have applied both requirements to both model simulations and scaled all data to a wavelength of 532nm. The CALIOP retrieval only reports the aerosol extinction coefficient for layers in which aerosol particulates were detected above the minimum retrieval limit and uses fill values for the rest of the profile. Therefore, it is important to note that the CALIOP sAOD could be biased towards large values of aerosol extinction during the first few months after the eruption and towards smaller values after the plume has become more diffuse.

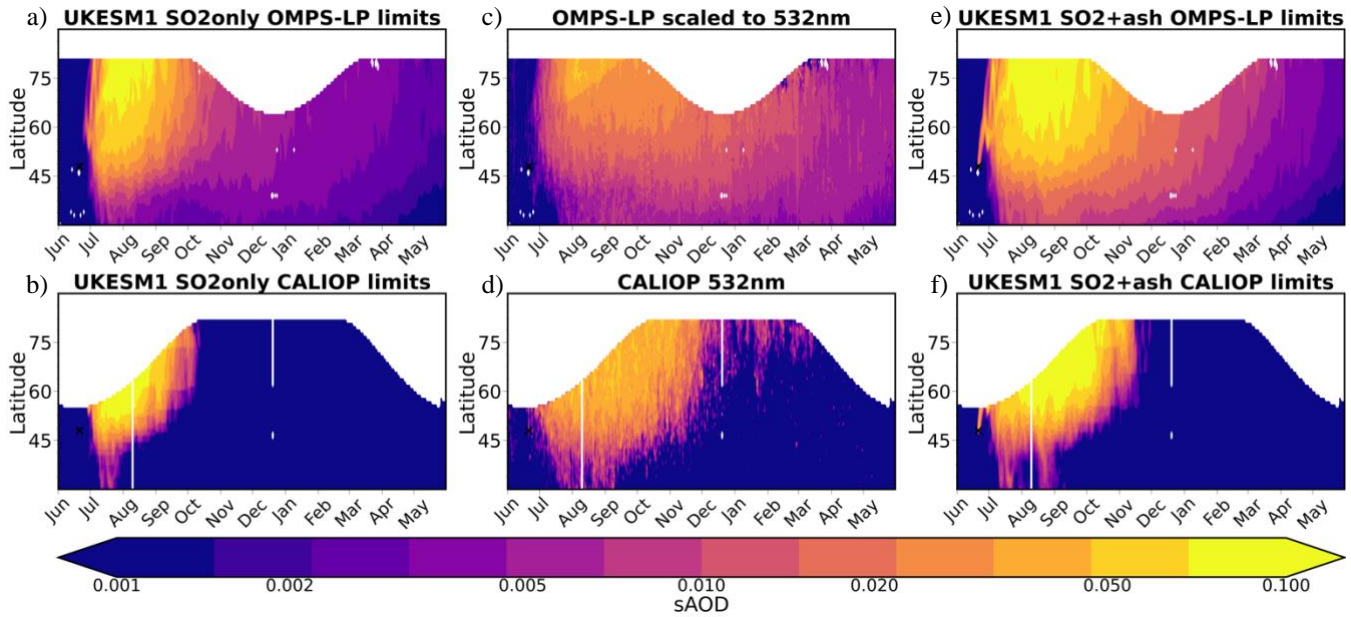


**Figure 4:** Latitude-time distribution of the zonally averaged sAOD from 30–90° N. (a) UKESM1 SO2only masked for OMPS-LP observations, scaled from 550nm to 532nm (b) UKESM1 SO2only masked for CALIOP observations, sAOD calculated with values of aerosol extinction  $< 0.012 \text{ km}^{-1}$ , the CALIOP minimum detection limit, scaled to 532nm (c) OMPS-LP observations scaled from 869nm to 532nm (d) CALIOP observations at 532nm (e) UKESM1 SO2+ash masked for OMPS-LP observations, scaled from 550nm to 532nm (f) UKESM1 SO2+ash masked for CALIOP observations, sAOD calculated with values of aerosol extinction  $< 0.012 \text{ km}^{-1}$ , the CALIOP minimum detection limit, scaled to 532nm. The location of Raikoke is marked with a black cross.

Fig. 4c shows the evolution of zonal mean sAOD derived from OMPS-LP from June 2019 to May 2020. The zonal peak sAOD occurs  $\sim 1.5$  months after the eruption, which is similar to the findings in Gorkavyi et al., 2021. The impact on the sAOD in OMPS-LP is still present one year later, with values of sAOD not yet returned to their pre-eruption values. This contrasts with Fig. 4d, the same quantity derived from CALIOP, where the perturbation of sAOD is significantly reduced by December 2019 and by March/April 2020 zonal sAOD values are similar to those found pre-eruption. We can confidently attribute this



difference in aerosol lifetime to the high aerosol extinction minimum detection threshold for aerosol extinction associated with the CALIOP dataset. Figs. 4b and 4f display the UKESM1 SO<sub>2</sub>only and SO<sub>2</sub>+ash zonal mean sAOD with the CALIOP minimum retrieval limits applied where a similar distribution to that seen in the observations is modelled, indicating that the shorter aerosol lifetime observed in the CALIOP retrievals compared to OMPS-LP is due to high detection limits. As the plume disperses over time the plume becomes more diffuse and becomes undetectable by CALIOP, leading to under-detection and hence the integrated sAOD reduces much more rapidly than we see in the OMPS-LP data which does not have the same high minimum detection threshold.

In both sets of observations (Figure 4c and 4d) we can see that the enhanced stratospheric aerosol layer has been transported poleward by the Brewer-Dobson circulation with the highest sAODs found north of the eruption. The model simulations represent this transport relatively well with similar distributions to both OMPS-LP and CALIOP observations. However, in all cases the peak magnitude is over estimated, especially in the SO<sub>2</sub>+ash case. Whilst the peak sAOD in the SO<sub>2</sub>only simulation (Fig. 4a and 4b) is less of an overestimate of the observations compared to SO<sub>2</sub>+ash, it does not reproduce the evolution of the plume as well as the SO<sub>2</sub>+ash simulation (Fig. 4e and 4f) in either case. Despite the SO<sub>2</sub>+ash simulation (Fig. 4f) representing the CALIOP retrievals well it is not representative of how the plume evolves over time after becoming too diffuse for CALIOP detection limits. However, as OMPS-LP has a much lower minimum detection threshold as a dedicated stratospheric limb-profiler the decay rate of sAOD is much slower. We see a similar decay rate in the SO<sub>2</sub>+ash simulation (Fig. 4e) with comparable magnitudes to the OMPS-LP observations from December onwards. From Fig. 4 we can begin to infer that the SO<sub>2</sub>+ash simulation represents the evolution of zonal sAOD better than the SO<sub>2</sub>only case, but this inference is far from conclusive. Further comparisons to the model are made in Sect. 4.4.

### 4.3 Temporal evolution of sulfate aerosol

The CALIOP and OMPS-LP derived perturbations of sAOD from the long-term mean are presented in Figure 5. As seen in Fig. 4 the two satellite observations have different temporal evolutions. Comparing the early stages of the plume evolution it is clear that OMPS-LP does not detect the same high peak in sAOD as CALIOP, however as previously mentioned the mean CALIOP sAOD could be biased towards higher values of aerosol extinction due to fill values below the minimum retrieval limit. The CALIOP dataset shows a clear peak 60 days after the eruption with an sAOD of approximately 0.026 whereas, OMPS-LP reaches a peak sAOD of approximately 0.015 over 3 months after the eruption. Studies have suggested that limb-instruments such as OMPS-LP can fail to detect aerosol near the tropopause (e.g., Fromm et al., 2014). However, since CALIOP is a nadir viewing lidar the altitude of the plume does not significantly affect the retrieval. This could contribute to the difference we see in the initial sAOD peaks since the plume was detected at altitudes as low as 11km (Hedelt et al., 2019; Vaughan et al., 2020). The vertical profile of the plume is explored further in Section 4.6. We also see a big difference in the decay rate of sAOD. The CALIOP observations have an *e*-folding time of 84 days, in comparison to OMPS-LP which has an *e*-folding time of 220 days. As previously discussed, the difference in decay rate between CALIOP and OMPS-LP is likely



435 due to the different minimum detection thresholds for both satellites. Once the plume begins to dilute and become more diffuse the higher CALIOP detection threshold ( $0.012 \text{ km}^{-1}$ ) results in under-detection in comparison to OMPS-LP which has a much lower threshold ( $1 \times 10^{-5} \text{ km}^{-1}$ ) and is thus able to detect more of the diffuse plume.

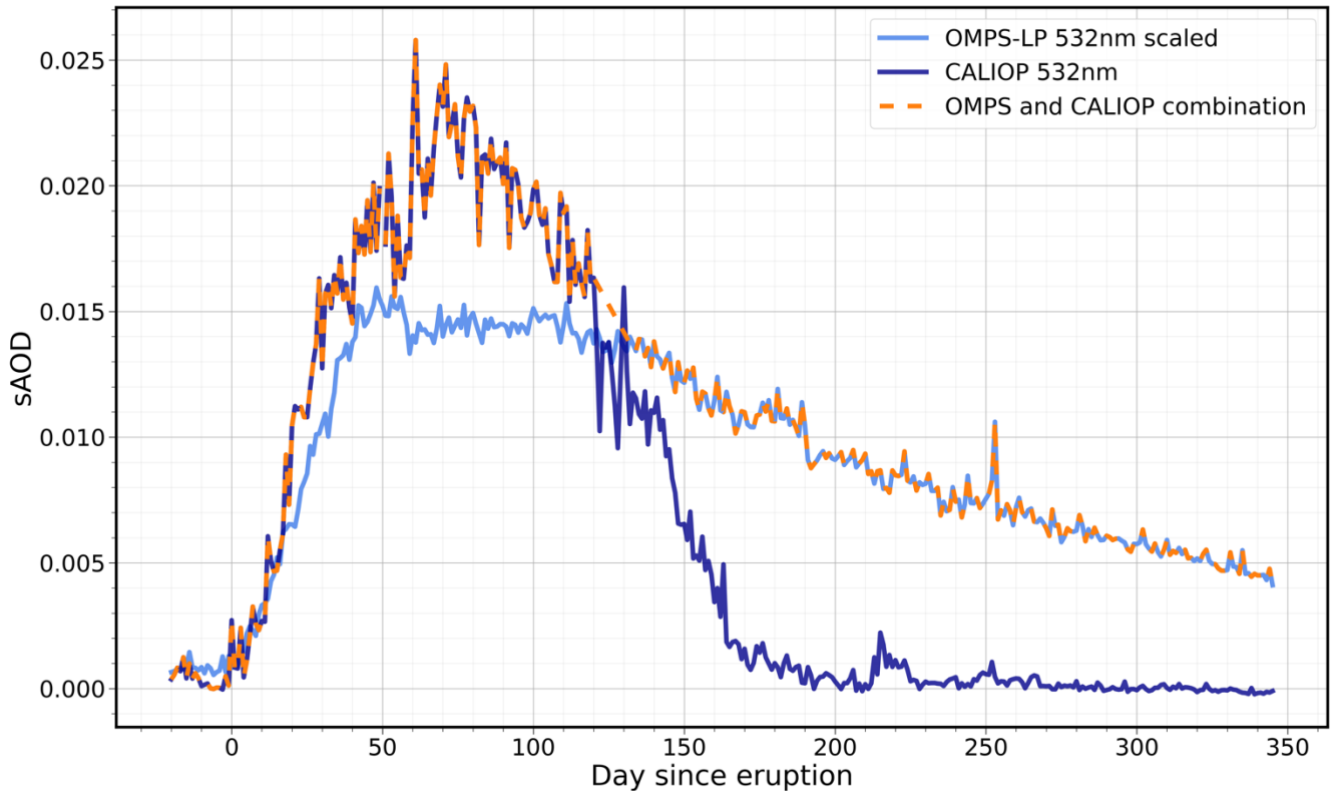


**Figure 5:** Daily perturbation in the sAOD averaged over  $30\text{--}90^\circ \text{ N}$  as observed by OMPS-LP scaled from  $510\text{nm}$  to  $532\text{nm}$  (light blue) and CALIOP at  $532\text{nm}$  (dark blue). The orange dashed line represents the combined OMPS-LP and CALIOP dataset at  $532\text{nm}$ . We remove the long-term background sAOD derived from OMPS-LP ( $0.0041$ ) and CALIOP ( $0.0003$ ) for the years 2013–2018 from those for 2019 to provide a stratospheric perturbation for the observations.

We have created a combined dataset which includes aerosol extinction data from both CALIOP and OMPS-LP, seen in Fig. 5. The combined dataset utilises the area averaged ( $30 - 90^\circ \text{N}$ ) CALIOP sAOD data for the first 4 months after the eruption before it is linearly interpolated over the region in which the two datasets cross over and then employs OMPS-LP data for the remaining months. This new dataset has an  $e$ -folding time of 145 days, and we believe that it is more physically reasonable than using a single observational dataset due to the data constraints outlined above. To confirm qualitatively that using the OMPS-LP data is more appropriate than CALIOP in the later months after the eruption we use in-situ ground-based data to provide an alternative comparison to these satellite datasets. We utilize the AERONET Level 2 AOD retrievals measured at

550nm and scale them to 532nm for comparison with the satellite observations. To calculate the satellite retrievals at MLO an area average is taken across multiple grid boxes encompassing the MLO. Note that AERONET retrievals of sAOD are not a point measurement as they are a function of the solar zenith angle. For solar zenith angles of 60-80 degrees and assuming that any aerosol is located in the lowest 20km above the observatory, aerosol within a 35-115km radius of the Mauna Loa observatory is included in the observations. The same area is used to calculate the average monthly SO<sub>2</sub>only and SO<sub>2</sub>+ash perturbations.

	AERONET	OMPS-LP	UKESM1 SO <sub>2</sub> only	UKESM1 SO <sub>2</sub> +ash
August	5.89 x 10 <sup>-3</sup>	<b>2.16 x 10<sup>-3</sup></b>	2.78 x 10 <sup>-3</sup>	4.27 x 10 <sup>-3</sup>
September	<b>12.12 x 10<sup>-3</sup></b>	<b>7.07 x 10<sup>-3</sup></b>	3.03 x 10 <sup>-3</sup>	8.46 x 10 <sup>-3</sup>
October	<b>9.78 x 10<sup>-3</sup></b>	<b>6.41 x 10<sup>-3</sup></b>	3.33 x 10 <sup>-3</sup>	7.12 x 10 <sup>-3</sup>
November	<b>4.70 x 10<sup>-3</sup></b>	<b>4.89 x 10<sup>-3</sup></b>	2.91 x 10 <sup>-3</sup>	5.40 x 10 <sup>-3</sup>
December	1.05 x 10 <sup>-3</sup>	<b>3.81 x 10<sup>-3</sup></b>	2.12 x 10 <sup>-3</sup>	3.96 x 10 <sup>-3</sup>
Average	6.71 x 10 <sup>-3</sup>	4.87 x 10 <sup>-3</sup>	2.83 x 10 <sup>-3</sup>	5.84 x 10 <sup>-3</sup>

**Table 3:** Perturbation of AOD from the long-term mean retrieved from the Mauna Loa Observatory AERONET site scaled to 532nm. OMPS-LP, UKESM1 SO<sub>2</sub>only and SO<sub>2</sub>+ash sAOD perturbation calculated across an area encompassing the MLO (19–20° N, 152–156° W). Observations highlighted with bold text are statistically significantly greater than the long-term mean at 95% confidence level. Negative values of AOD are a result of calculating the perturbation from the long-term mean (2013–2018).

Average monthly perturbations from the long-term mean (or control simulation) for the Mauna Loa observatory, are presented in Table 3. The AERONET retrievals are statistically significant at the 5% level from the long-term mean from September to November and increase to a peak AOD of 12.12 x 10<sup>-3</sup> in September, over 2 months after the eruption. The OMPS-LP retrievals and SO<sub>2</sub>+ash model show a similar pattern with peak AODs in September of 7.07 x 10<sup>-3</sup> (OMPS-LP) and 8.46 x 10<sup>-3</sup> (SO<sub>2</sub>+ash). The SO<sub>2</sub>only simulation follows a similar pattern of increased AOD between August and November, however the magnitude of AOD is much smaller than the AERONET and OMPS-LP observations. OMPS-LP retrievals are also significantly greater than the long-term mean from August through until December. CALIOP however does not appear to detect any statistically significant perturbation to the sAOD, with values an order of 10<sup>2</sup> smaller than those observed by AERONET and OMPS-LP. This is most likely due to aerosol loadings falling below the minimum detection threshold and the plume becoming more diffuse at this latitude. We also calculate the model average perturbed AOD for this region from August

to December, presented in Table 3. The SO<sub>2</sub>+ash average AOD,  $5.84 \times 10^{-3}$ , agrees well with the AERONET and OMPS-LP  
475 observations,  $6.71 \times 10^{-3}$  and  $4.87 \times 10^{-3}$  respectively. However, the SO<sub>2</sub>only average AOD is much smaller suggesting that  
the SO<sub>2</sub>+ash simulation validates better against this specific set of observations.

MLO is located at 19.5°N, around 30° south of Raikoke. Due to its proximity to the 5°S Ulawun eruption, there is the potential  
for this eruption to influence observational data. Model simulations were run without Ulawun emissions (discussed further in  
480 Sect. 4.7) and a negligible influence on the AOD in the MLO region over this time period was observed. While there may  
indeed be an influence from Ulawan on the AODs determined at Mauna Loa in the observational record, this modelling and  
the observed timing of the statistically significant AOD perturbations suggest that any influence is small. As we noted in Fig.  
4 most of the aerosol plume travelled poleward via the Brewer-Dobson circulation, however there was some southern transport  
seen in both satellite observations in late July and August. We can observe this further in Figure 6, the monthly average sAOD  
485 observed by OMPS-LP and CALIOP.

A similar analysis performed by Haywood et al. (2010) for the Sarychev eruption reveals 550nm AOD perturbations of +0.010  
and +0.008 for July and August. Given that the Sarychev and Raikoke eruptions occurred within a few calendar days of each  
other but in different years, it appears that the equatorward transport of aerosol for the Sarychev eruption was quicker than for  
490 the Raikoke eruption. This conclusion holds despite any potential influence from the eruption of Ulawun and highlights that  
considerable differences in transport can occur for volcanic eruptions that are ostensibly very similar in terms of latitude,  
timing, injection amount and vertical distribution (Jones et al., 2016).

Figure 6 shows the monthly geographic evolution of the sAOD in the Northern Hemisphere. MLO is highlighted on the first  
495 plot by a red cross. From this plot we can see that transport to lower latitudes does not occur until August, however the CALIOP  
retrievals are much more diffuse than those observed in OMPS-LP. We observe high values of sAOD at high latitudes with  
peaks across Greenland and Northern Canada. Despite the missing data in the CALIOP observations we can still see a  
reasonable spatial agreement in the sAOD during the first few months. In October an interesting feature is seen in the OMPS-  
LP data where a band of enhanced sAOD is observed between 0 – 15°N. This might be attributed to the second Ulawun  
500 (5.05°S, 151°E) eruption on 3<sup>rd</sup> August which, owing to the latitude and altitude of the eruption is likely to be confined by the  
so-called “tropical pipe” between approximately 15°S-15°N (e.g. Plumb, 1997), although some leakage to higher latitudes  
might be expected over time. From August onwards the stratospheric aerosol layer south of the equator has been shown to  
become enhanced. Kloss et al., (2021) estimate that the aerosol from the Ulawun eruption circled the Earth in the tropics within  
one month. During October and November the sAOD in the tropical stratosphere becomes increasingly enhanced, which is  
505 likely due to the influence of Ulawun. Due to the influence of Ulawun this study uses area averages from 30 – 90°N to ensure  
analysis focuses solely on the impact of the Raikoke eruption. Despite the potential influence of Ulawun on MLO observations,  
we can nevertheless conclude that combining the initial CALIOP peak and the latter half of the OMPS-LP data is the most

appropriate representation of the plume evolution since OMPS-LP does not observe the initial peak while CALIOP detection limits lead to non-detection of aerosol once it has become diffuse hence apparently reducing the observed lifetime and e-  
510 folding time of the sulfate aerosol.

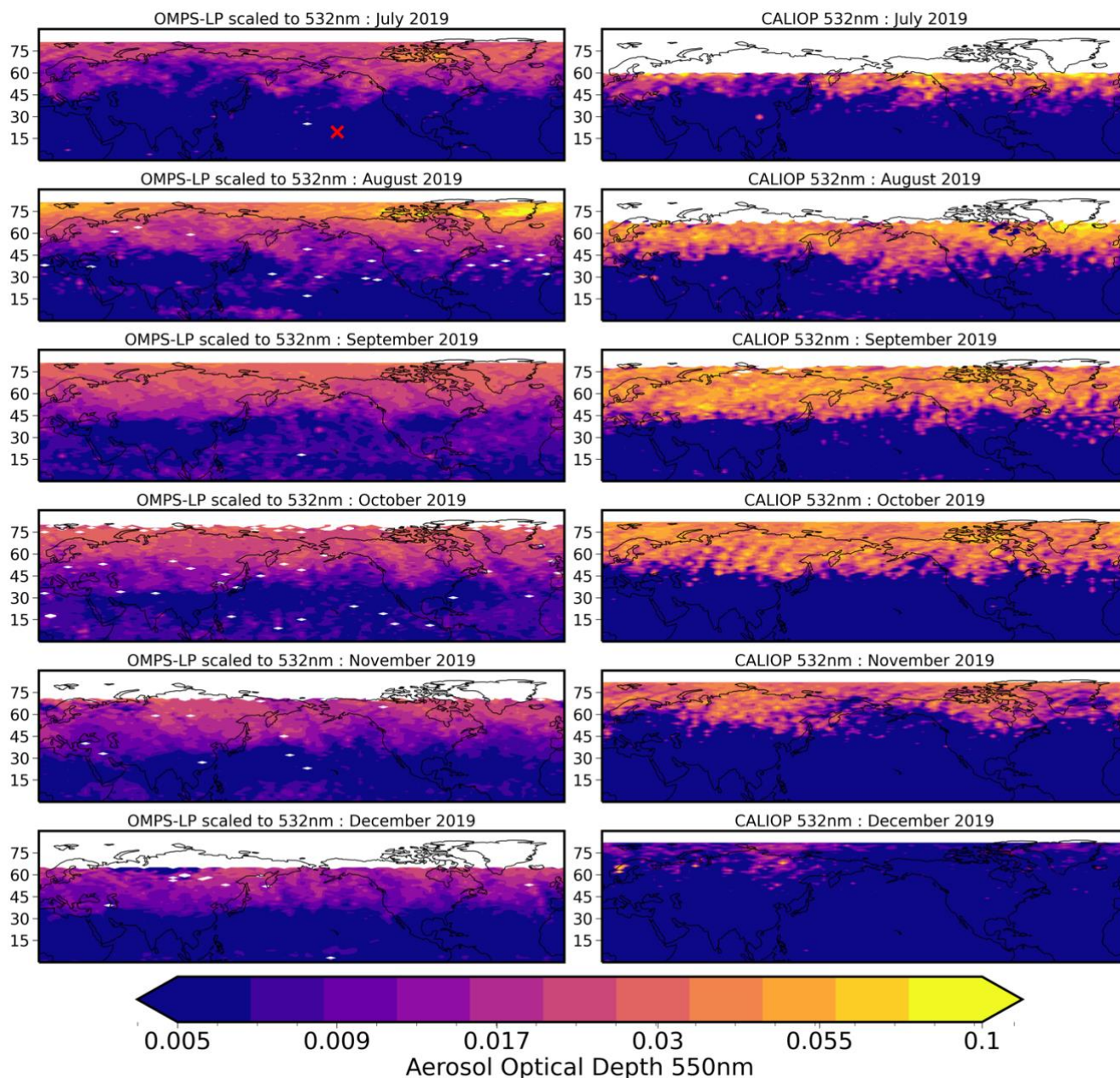


**Figure 6:** Monthly geographic evolution of the Northern Hemisphere sAOD from July 2019 to December 2019 derived from OMPS-LP Retrieved Aerosol Extinction (left) and CALIOP Aerosol Extinction Profile (right). We remove the long-term

background sAOD derived from OMPS-LP and CALIOP for the years 2013–2018 from those for 2019 to provide a  
515 stratospheric perturbation for the observations.

#### 4.4 Model comparison

To make consistent and accurate comparisons between the combined satellite dataset and the model simulations it is  
appropriate to implement the same method used in Fig. 4 and apply minimum detection and spatial limits to the model data.  
Figure 7 compares the combined OMPS-LP and CALIOP dataset to the two model simulations both with (solid lines) and  
520 without (dashed lines) the respective observational limits applied. For the first 4 months after the eruption the combined dataset  
uses the CALIOP observations, therefore we use the CALIOP minimum detection threshold ( $0.012 \text{ km}^{-1}$ ) to filter out aerosol  
extinction values in the model simulations before calculating the sAOD for comparison. After this we apply the limits of the  
OMPS-LP data to the model simulations in a similar fashion since OMPS-LP is used in the combined observational dataset  
for the following months. For both SO<sub>2</sub>only and SO<sub>2</sub>+ash we only include model data where observational data were available.  
525 When the observational limits were applied, no linear interpolation across the location where the combined dataset switches  
from CALIOP to OMPS-LP was applied to the model simulations owing to the considerable difference in sAOD across the  
area of interpolation.

Figure 7 clearly demonstrates significant differences between the sulfate aerosol evolution in the SO<sub>2</sub>only and SO<sub>2</sub>+ash  
530 simulations. Considering first the SO<sub>2</sub>only simulations, we note that the timing of the peak is much earlier in SO<sub>2</sub>only  
compared to the observations. The combined observational dataset peaks at approximately 0.026 around 2 months after the  
eruption and has an *e*-folding time of 145 days. For the SO<sub>2</sub>only simulations when including the observational limits, which  
is considered the most appropriate method of comparison, the peak sAOD is much greater (0.033) and earlier than observations.  
We observe a similarly fast decrease in sAOD when observational limits are applied to SO<sub>2</sub>only (*e*-folding time of 45 days),  
535 whereby the sAOD drops to values close to zero at day 110 before an increase at approximately day 125 after the eruption.  
This abrupt change is an artifact of combining CALIOP and OMPS-LP limits to the SO<sub>2</sub>only simulation to best compare  
against the combined observational dataset.

Now considering the SO<sub>2</sub>+ash simulations. In contrast to the SO<sub>2</sub>only simulation, there is a large difference in the first 50  
540 days after the eruption between the SO<sub>2</sub>+ash model with and without limits. When observational limits are applied (as  
recommended), the peak sAOD (0.042), whilst still an overestimate, occurs 60 days after the eruption which is more consistent  
with the combined observational dataset. The delay in the peak of sAOD when observational limits are applied can be attributed  
in part to the missing data at high latitudes during the polar summer since we can still identify this delay in the peak sAOD  
when we only apply spatial CALIOP limits to SO<sub>2</sub>+ash. We can see in both Fig. 4 and 6 the sulfate aerosol travels poleward  
545 due to the Brewer-Dobson circulation and we would expect the resulting sAOD to be greatest within the first few months after

the eruption. However, since the months following the eruption are the Northern Hemisphere summer, there are no CALIOP night retrievals at high latitudes, contributing to the appearance of a delayed sAOD peak.

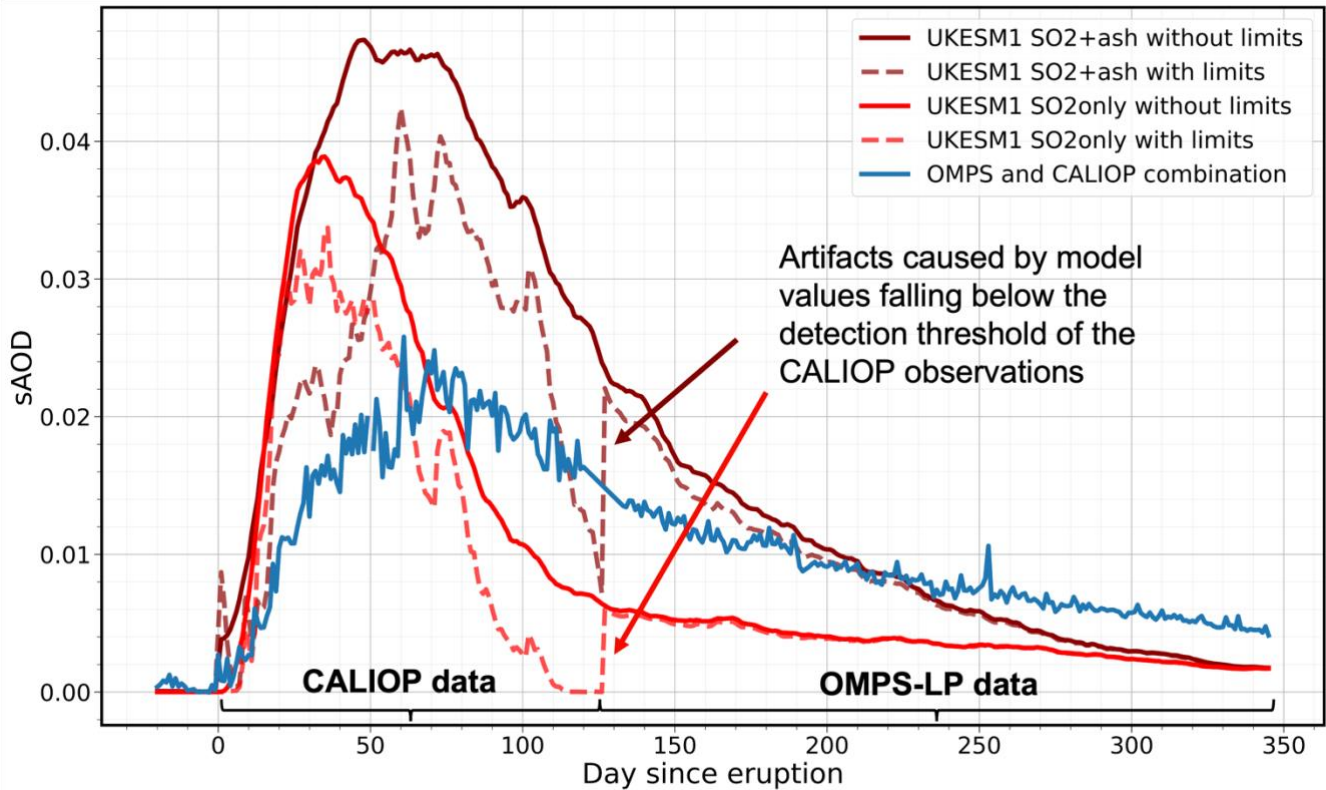


**Figure 7:** Daily perturbation of sAOD at 532nm averaged over 30–90° N. Daily OMPS-LP and CALIOP combined dataset sAOD (blue), UKESM1 SO<sub>2</sub>only with observational limits applied (red) and without limits applied (red dashed) and UKESM1 SO<sub>2</sub>+ash with observational limits applied (dark red) and without limits applied (dark red dashed). We remove the long-term background sAOD derived from OMPS-LP and CALIOP for the years 2013–2018 from those for 2019 to provide a stratospheric perturbation for the observations. Similarly, we remove the impacts of background stratospheric aerosol from the model simulations by subtracting the sAOD from the CNTL simulation from those for SO<sub>2</sub>only and SO<sub>2</sub>+ash.

555

When observational limits are applied to SO<sub>2</sub>+ash we observe a decline in model sAOD after the peak owing to transfer from the stratosphere to the troposphere with an  $e$ -folding time of 90 days, almost 2 months faster than the observed data. The initial steep decline in SO<sub>2</sub>+ash is due to the CALIOP limits imposed upon the model. At approximately day 135 after the eruption there is a sharp increase in modelled sAOD. This is an artifact of combining SO<sub>2</sub>+ash with CALIOP limits and SO<sub>2</sub>+ash with OMPS-LP limits. The SO<sub>2</sub>+ash simulation with CALIOP limits applied has a much faster decay rate with an  $e$ -folding time of 44 days, whereas the SO<sub>2</sub>+ash simulation with OMPS-LP limits has a much longer  $e$ -folding time of 101 days. Whilst

560



SO<sub>2</sub>+ash is not perfect at recreating the sAOD evolution, we can see that by applying the observational limits it starts to become apparent that SO<sub>2</sub>+ash provides a better comparison against observations than SO<sub>2</sub>only, although some considerable differences still exist. In the following two sections we explore changes to the stratospheric aerosol Ångström Exponent and the vertical profile evolution of the aerosol to further examine the consistency of the SO<sub>2</sub>only and SO<sub>2</sub>+ash simulations against observations.

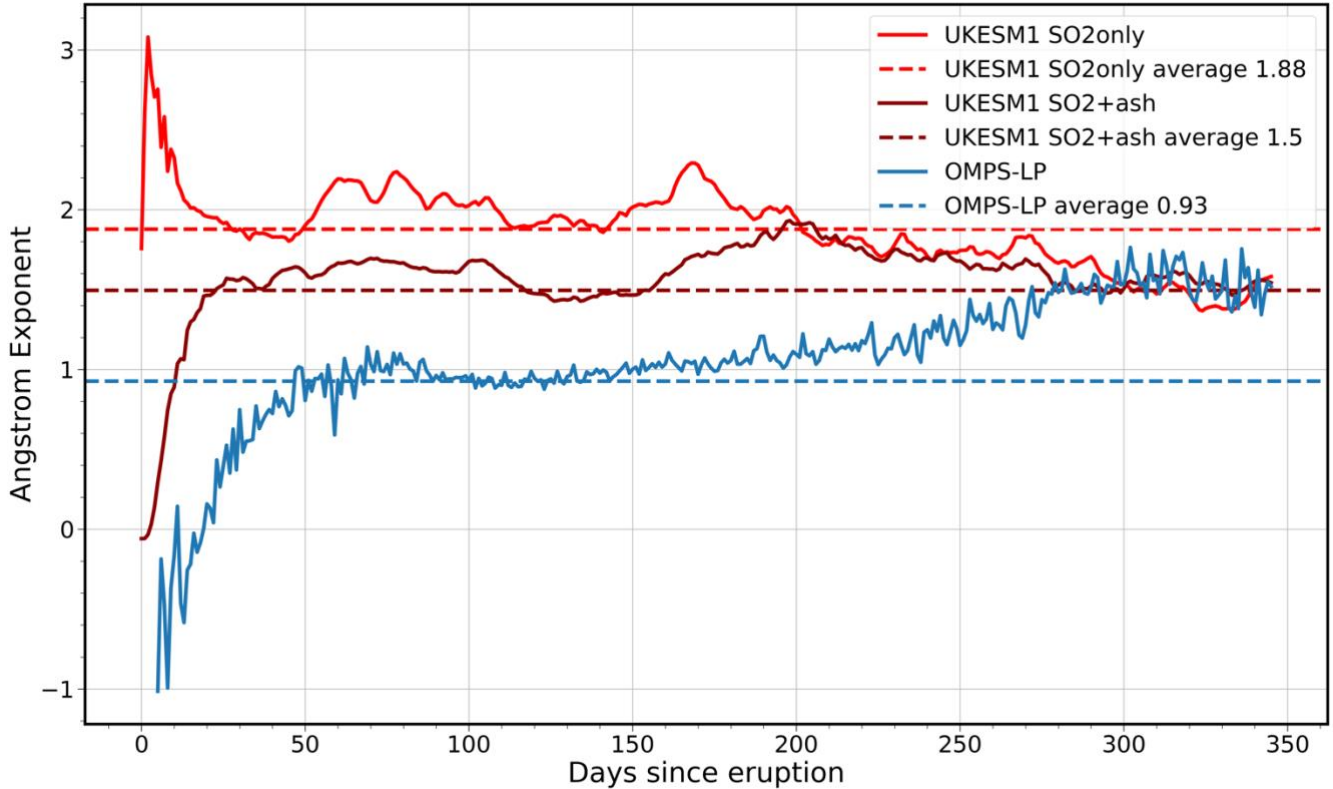


**Figure 8:** Daily evolution of Ångström Exponent for OMPS-LP (blue), UKESM1 SO<sub>2</sub>only (red) and UKESM1 SO<sub>2</sub>+ash (dark red). Calculated using area weighted sAOD between 30–90° N (same as Fig. 7) using 510nm and 869nm wavelengths.

#### 570 4.5 Analysis of stratospheric aerosol Ångström Exponents

Without detailed in-situ measurements (e.g. Jégou et al., 2013) it is not possible to know with a high level of accuracy, the detailed size distribution of the volcanic aerosols. However, the wavelength dependence can be used to calculate the Ångström Exponent, since it is often used as an indicator of aerosol particle size. For measurements of optical depth  $\tau$  and at wavelengths  $\lambda_1$  and  $\lambda_2$  the Ångström Exponent is given by Eq. (1):

$$575 \quad \alpha = - \log \frac{\tau_{\lambda_1}}{\tau_{\lambda_2}} / \log \frac{\lambda_1}{\lambda_2}, \quad (1)$$

The OMPS-LP aerosol extinction measurements are provided at wavelengths ranging between 510 – 997nm, presenting the opportunity to calculate the sAOD and analyse the evolution of the Ångström Exponent and consequently variations in the aerosol size distribution after the eruption. Figure 8 shows the daily Ångström Exponent (AE) for OMPS-LP, SO<sub>2</sub>only and SO<sub>2</sub>+ash calculated using the area averaged sAOD at wavelengths 510nm and 869nm between 30 – 90°N.

580

The observations show that the AE is initially close to between -1 and 0 indicating that large particles were observed immediately after the eruption, and therefore contains a significant amount of volcanic ash. After around 50 days after the eruption, the AE increases to approximately 1 for a period of over 3 months, this could suggest that the largest particles had dropped out and smaller particles remained. As the time after the eruption increases, the AE increases to a maximum value of ~1.6. Kloss et al., 2021 estimate a pristine average AE of 1.7 using background sAODs which suggests that approximately 300 days after the eruption the observations have returned to pre-eruption AE average.

585

590

Both model simulations converge on an AE of around 1.6 after 300 days, however they both display starkly contrasting behaviour immediately after the eruption. In the SO<sub>2</sub>only scenario the initial AE is very high (up to around 3) indicating smaller particles and decreases with time. The behaviour of the AE is therefore the opposite of what is observed.

595

600

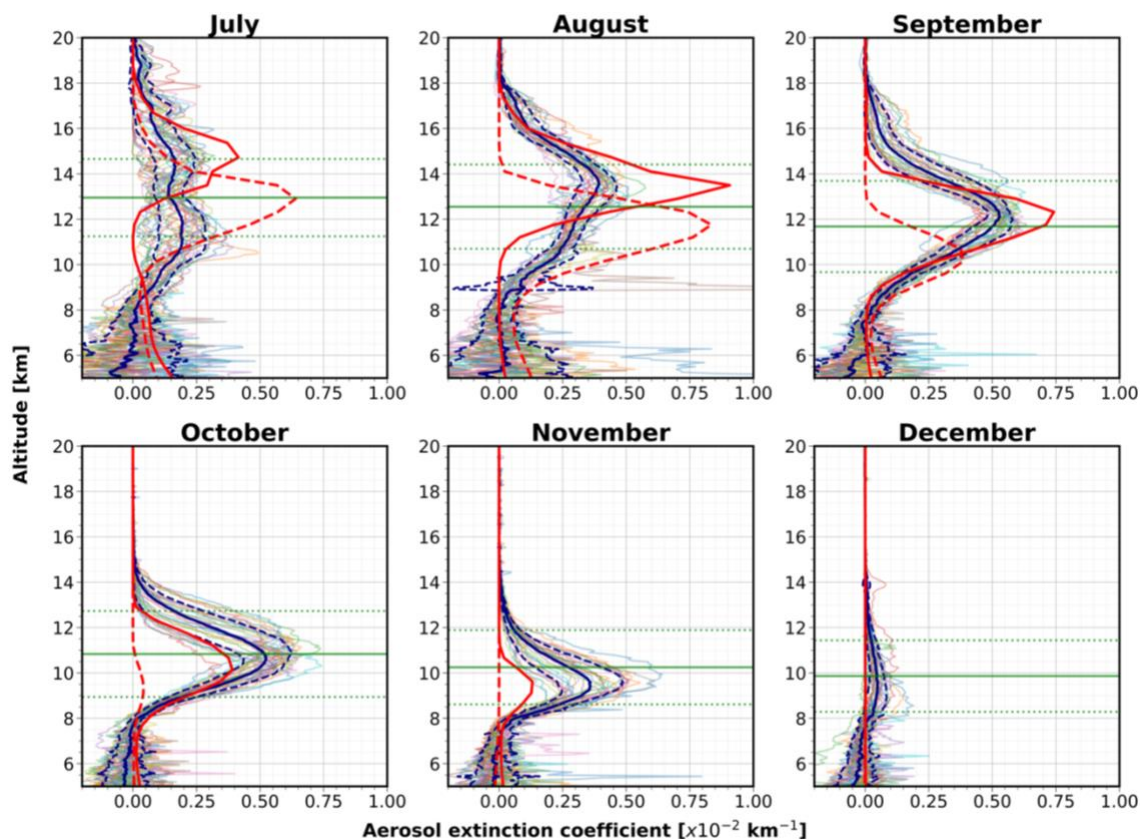
In comparison, during the first 10 days after the eruption, the SO<sub>2</sub>+ash scenario shows an AE of around zero initially owing to the presence of ash, which then increases as the ash falls out from the atmosphere. This behaviour is much more similar to what we see in the observations as compared to SO<sub>2</sub>only, confirming that our SO<sub>2</sub>+ash simulations are in better agreement with observations. However, the agreement is far from perfect with the model AE increasing much faster than what we see in the observations, it then converges with the SO<sub>2</sub>only scenario approximately 200 days after the eruption. Considering an internal mixture between ash and sulfate in the model could potentially resolve the differences between the observations and the model AE. However, the slower increase in the observed AE could also indicate an influence from pumice or soot particles from forest fires. Despite these differences, this figure again suggests that the SO<sub>2</sub>+ash scenario is better at representing the observations compared to the SO<sub>2</sub>only case. Further discussion of this is provided in Sect. 5.

#### 4.6 Aerosol extinction vertical profile analysis

605

Figure 9 shows the vertical evolution of the CALIOP derived aerosol extinction coefficient with monthly averages and standard deviation from July until December. We also include both model simulations, SO<sub>2</sub>only (dashed red line) and SO<sub>2</sub>+ash (solid red line) for comparison. The observed monthly tropopause height (mean and standard deviation) is also included to highlight tropospheric and stratospheric altitudes. Both observations and model simulations are averaged over 30 – 90°N, not including those latitudes where CALIOP night retrievals are unable to retrieve data due to polar summer. Since CALIOP aerosol extinction retrievals have a minimum detection threshold of 0.012 km<sup>-1</sup> (Toth et al., 2018) this limit has also been applied to the SO<sub>2</sub>only and SO<sub>2</sub>+ash data for a more consistent comparison.





610 **Figure 9:** Aerosol extinction coefficient vertical profile averaged longitudinally and over 30–90° N. Averaged daily CALIOP  
 aerosol extinction coefficient vertical profiles (night retrievals only, fainter lines) with monthly average (bold blue) and  
 615 monthly average plus/minus standard deviation (solid dashed black lines). UKESM1 SO<sub>2</sub>+ash (solid bold red) and SO<sub>2</sub> only  
 (dashed bold red) simulations with imposed CALIOP minimum retrieval limits and mask. Average tropopause height is shown  
 by the horizontal green line and the average tropopause height +/- one standard deviation for 2019 is also shown in green  
 dotted lines.

In the CALIOP observations we can see that initially after the eruption there are two peaks at ~11km and ~14.5km similar to  
 the two injection altitudes used to initialise the UKESM1 simulations. The observations then form a singular peak above the  
 average tropopause at ~14km which increases in magnitude to a peak of  $5.3 \times 10^{-3} \text{ km}^{-1}$  between September and October. In  
 620 comparison, the two model simulations peak at  $8.3 \times 10^{-3} \text{ km}^{-1}$  for SO<sub>2</sub>only at ~12km and  $9.1 \times 10^{-3} \text{ km}^{-1}$  for SO<sub>2</sub>+ash at ~13.5km.  
 We notice a considerable difference in the altitude of the plume between the two model simulations. In July the peak aerosol  
 extinction for SO<sub>2</sub>only is at approximately 13km, a similar altitude to the average tropopause height. In contrast to this, the  
 SO<sub>2</sub>+ash plume has a peak aerosol extinction at ~15km. This initial difference in height results in a significant impact on the  
 lifetime of the aerosol. To explore the impact of the altitude of the plume further, we look at Figure 10 which displays the

625 aerosol extinction coefficient as a function of latitude and altitude. This avoids averaging over a widely varying tropopause height and allows us to examine the altitude of the plume in the models and observations against the altitude of the tropopause and how it might affect the aerosol lifetime.

As per the analysis shown in Fig. 9, we impose the CALIOP detection limits onto the model simulations and only include  
630 latitudes in which CALIOP data is available. The average monthly tropopause height is included and shown by the black line. The initial difference between the plume altitude of SO<sub>2</sub>only and SO<sub>2</sub>+ash is striking. Already in July we observe some aerosol in the midlatitudes below the monthly tropopause height, with a substantial portion below the tropopause in August. However, we do not see this in the SO<sub>2</sub>+ash model until September and October. The CALIOP observations reveal the poleward transport of the aerosol via the Brewer-Dobson circulation from July through until September. This is reproduced reasonably well in the  
635 SO<sub>2</sub>+ash model, however we do not observe this in the SO<sub>2</sub>only simulation. Similarly, the magnitude and spatial distribution of the aerosol in October is well modelled by SO<sub>2</sub>+ash compared to SO<sub>2</sub>only in which only a negligible aerosol extinction coefficient is found.

Due to more removal processes in the troposphere the altitude of the plume in relation to the tropopause height can impact the  
640 decay rate and lifetime of the aerosol. Since both model scenarios were initialised with the same SO<sub>2</sub> injection altitudes the difference between plume altitudes in July must be due to the self-lofting effect from the ash. Muser et al., 2020 had documented this for the Raikoke plume and noted that the maximum cloud-top height rose more than 6km within the first few days after the eruption. Whilst the SO<sub>2</sub>+ash scenario overestimates the magnitude of the aerosol extinction coefficient in the first few months, it does represent the altitude and lifetime of the aerosol plume well. The impact of the self-lofting effect is  
645 also seen in Fig. S2, which displays the stratospheric aerosol optical depth of SO<sub>2</sub>+ash and SO<sub>2</sub>only, alongside the sAOD derived from the CLASSIC dust emission and SO<sub>2</sub>+ash minus the sAOD from dust. We can see here that the impact from the ash itself is relatively negligible and therefore it must be the impact the ash has on the sulfate aerosol which drives the changes seen in sAOD.

650 The vertical profile analysis of the CALIOP aerosol extinction coefficient indicates how close the volcanic plume was to the tropopause in the first month or so after the eruption. This could explain why the OMPS-LP dataset missed the initial sAOD peak since limb-instruments can fail to detect aerosol near the tropopause (e.g. Fromm et al., 2014). Analysis of the aerosol size evolution and vertical profile in the model simulations have confirmed that the UKESM1 SO<sub>2</sub>+ash simulation is more consistent with the observations. Figs. 8, 9 and 10 illustrate that SO<sub>2</sub>+ash provides a much better representation of the aerosol  
655 size and lifetime and therefore resulting climatic impact than the SO<sub>2</sub>only scenario.

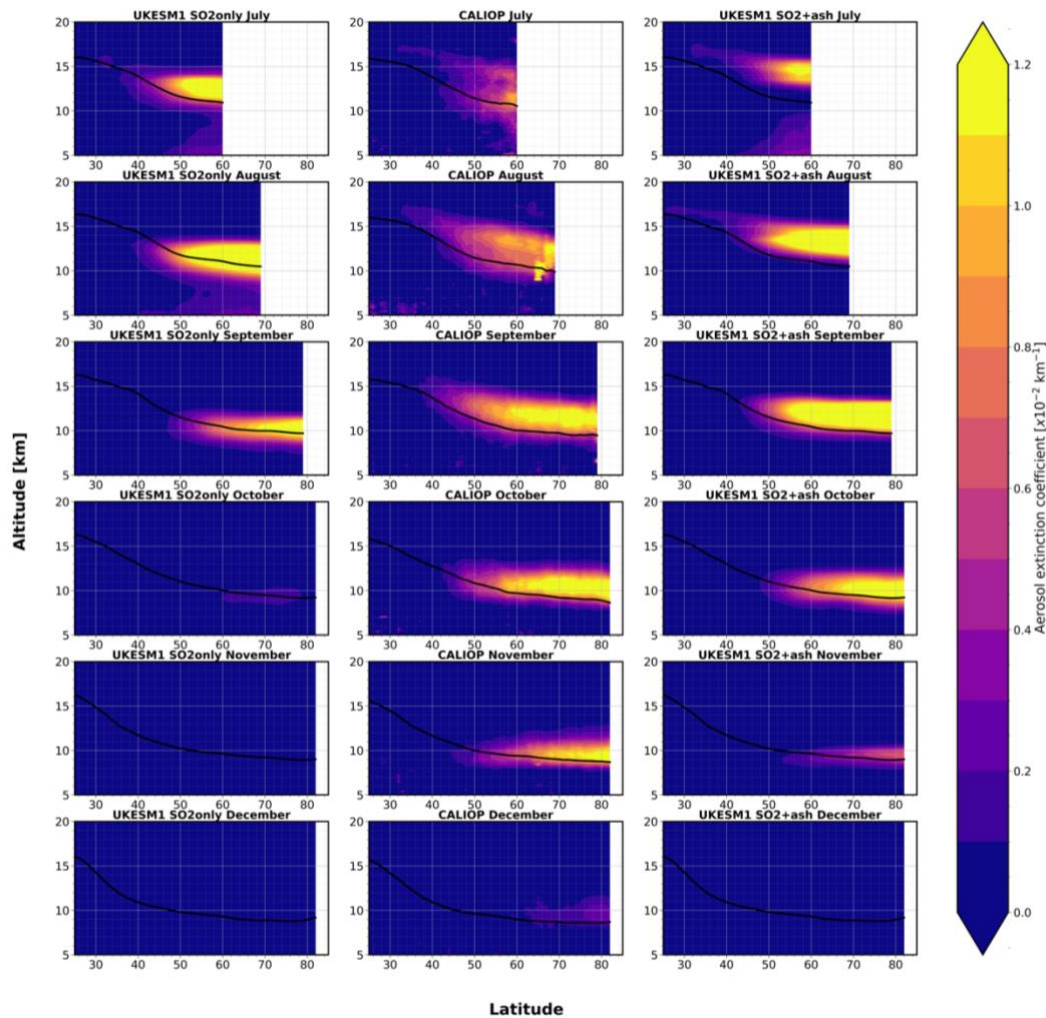


**Figure 10:** Aerosol extinction coefficient vertical profile averaged longitudinally. Averaged monthly CALIOP (centre) aerosol extinction coefficient vertical profiles (night retrievals only) with monthly average tropopause height (solid black). UKESM1 SO<sub>2</sub> only (left) and SO<sub>2</sub>+ash (right) simulations with imposed CALIOP minimum retrieval limits and mask.

#### 4.7 Radiative forcing

Haywood et al., 2010 ran simulations of the Sarychev eruption over a three-month period June-August 2009 and explored the difference between the aerosol optical depth and radiative forcing due to anthropogenic aerosol and the Sarychev Peak stratospheric aerosol plume. They found that in some regions of the NH the AOD was of comparable magnitude or greater than the AOD from anthropogenic emissions. We estimate the impact of the Raikoke eruption on the approximate radiative forcing exerted by the volcanic aerosol and compare this to the Sarychev Peak eruption. In Figure 11 we have recreated the

Sarychev Peak AOD and radiative forcing plots from Haywood et al., 2010 Figure 12 using data from HadGEM2 and compare them against our UKESM1 Raikoke simulations, eliminating the impacts of the Ulawun eruption. As in the results presented by Haywood et al. (2010), our UKESM1 simulations are nudged to reanalysis data, but the evolution of the control and experiment simulations differ slightly and result in some differences in the cloud and fields. Due to this, the all-sky radiative forcing cannot be accurately determined from the difference in the top of the atmosphere shortwave upwelling radiation with and without aerosols. The all-sky shortwave radiative forcing can be approximated for purely scattering aerosol, following the calculation used by Haywood et al., (2010), using the following equation, Eq. (2):

$$675 \text{ Radiative forcing} \approx (SW_{CTL} - SW_{EXP}) * (1 - A_c), \quad (2)$$

where  $SW$  is the clear-sky outgoing shortwave radiation ( $Wm^{-2}$ ) at the top of the atmosphere (TOA) for the control (CTL) and experiment (EXP) and  $A_c$  is the cloud fraction (Haywood et al., 1997). This assumes that the contribution from longwave radiation and the radiative forcing from cloudy areas is negligible. It has been shown through radiative transfer calculations that for conservative scattering from sulfate aerosols for optically thick cloud that this is a reasonable assumption (e.g. Haywood and Shine, 1997).

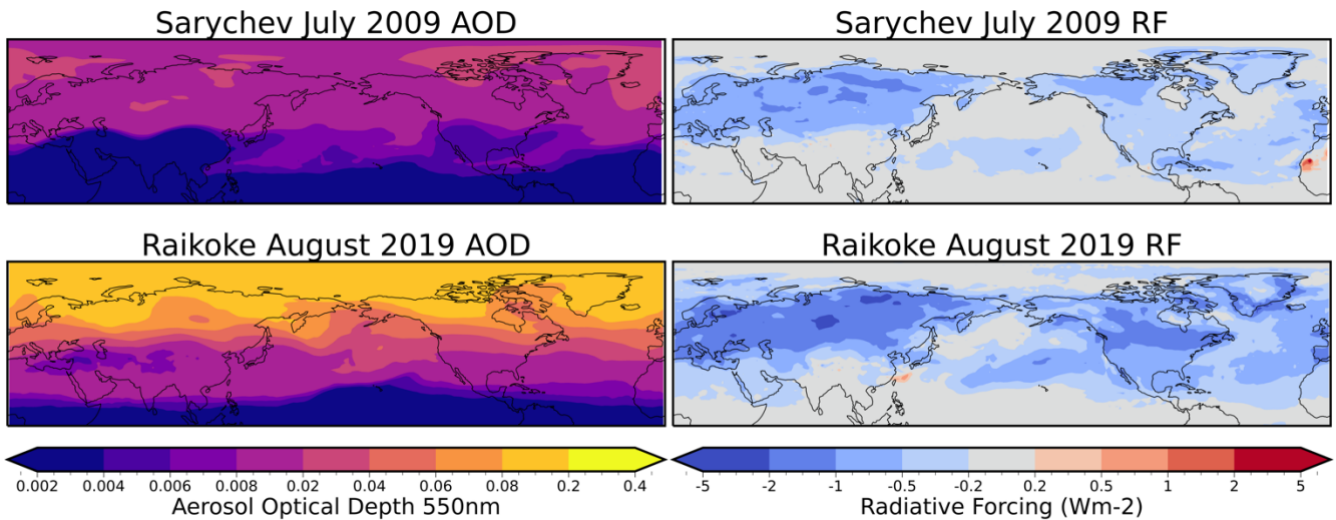


**Figure 11:** The sAOD for July at 550nm for a) Sarychev Peak derived from HadGEM2 and b) Raikoke derived from UKESM1. The cloud-free radiative forcing at the top of the atmosphere ( $Wm^{-2}$ ) for c) Sarychev Peak derived from HadGEM2 and d) Raikoke derived from UKESM1.

Figure 11 shows the months in which the different eruptions peak in both AOD and radiative forcing. In order to make global comparisons between the Sarychev Peak eruption and Raikoke, we perform a UKESM1 simulation in which we do not include the Ulawun eruption. We see in both plots that the Raikoke eruption had a greater impact on the global AOD and resulted in a

690 larger cloud-free radiative forcing at its peak. After the Sarychev Peak eruption the NH average AOD peaked in July at approximately 0.01, this is in comparison to Raikoke, where the peak NH averaged AOD occurred in August at approximately 0.03. The global and NH radiative forcing impacts from both eruptions from June through until August are shown in Table 4.

	Raikoke SO <sub>2</sub> only	<b>Raikoke SO<sub>2</sub>+ash</b>	Sarychev Peak
June	-0.001	<b>-0.004</b>	-0.03
July	-0.26	<b>-0.22</b>	-0.13
August	-0.29	<b>-0.25</b>	-0.07
September	-0.13	<b>-0.19</b>	N/A
October	-0.05	<b>-0.14</b>	N/A
November	-0.02	<b>-0.07</b>	N/A

695 **Table 4:** The cloud-free global mean radiative forcing (in Wm<sup>-2</sup>) at the top of the atmosphere for Sarychev Peak (after Haywood et al., 2010) derived from HadGEM2 and for Raikoke SO<sub>2</sub>only and SO<sub>2</sub>+ash simulations derived from UKESM1. N/A indicates not available.

700 Rather counter-intuitively, the cloud-free radiative forcing is some 20% stronger for the SO<sub>2</sub>only simulations than for the SO<sub>2</sub>+ash simulations. The explanation for this result is that, as in the case for clouds, the evolution of the aerosol differs slightly between the SO<sub>2</sub>only and the SO<sub>2</sub>+ash simulations. This results in sAODs that are some 20% larger over areas of central Eurasia in July and August, which are predominantly cloud-free in the model at that time of year. This results in cloud-free radiative forcings that are a factor of 1.2 greater for the SO<sub>2</sub>only simulations than the SO<sub>2</sub>+ash simulations. However, far greater fractional differences of up to a factor of 3.5 are evident in subsequent months owing to the general reduction in the sAOD documented in previous sections.

705 While the cloud-free radiative forcing from June cannot be directly compared owing to differences in timing of the eruptions (Sarychev eruption initiated 15<sup>th</sup> June in Haywood et al., (2010), but 21<sup>st</sup> June in this study), the global mean cloud-free radiative forcing from the Raikoke eruption in comparison to the Sarychev Peak eruption are substantially greater in July and August. At their peaks, the NH cloud-free radiative forcing of Raikoke is -0.48 Wm<sup>-2</sup>, almost twice as strong as that of Sarychev Peak (-0.24 Wm<sup>-2</sup>). This is due to a combination of factors including but not limited to i) the base-state model (UKESM1 versus HadGEM2), ii) the aerosol modelling scheme (UKCA versus CLASSIC), iii) differences in assumed vertical emission profile (80% at 13-15km versus evenly distributed between 11-15km), iv) differing meteorological conditions which have been shown to significantly impact aerosol distribution, lifetime, and hence radiative forcing, particularly for emissions close to the tropopause (Jones et al., 2016). Note that the inclusion of volcanic ash does not appear to be a significant cause of the

715 increased peak radiative forcing compared to the Sarychev analysis; the inclusion of ash appears to have a greater impact on  
the longevity of the radiative forcing through enhanced stratospheric aerosol lifetime. To fully evaluate differences across  
model formulations would require re-runs of the model for the Sarychev case with UKESM1, which is beyond the scope of  
this study.

## 5. Summary and conclusion

720 This study provides an analysis of satellite and ground-based observational data to determine if including ash in model  
simulations of volcanic eruptions can more accurately represent aerosol size, geographic distribution, and the evolution of  
volcanic plumes. There are substantial differences between observations due to different observational limitations. Whilst  
these were difficult to reconcile, we were able to apply numerous observational thresholds to UKESM1 to assess the ability of  
the model to replicate observations. Using multiple remote sensing methods we were able to validate the transport of the SO<sub>2</sub>  
725 plume, the evolution of the sulfate aerosol and associated radiative impacts modelled by the UKESM1 nudged to ERA5  
reanalysis data.

The Raikoke eruption was the largest volcanic injection of SO<sub>2</sub> into the stratosphere since the OMPS satellite was launched  
and was well observed by OMPS-NM and OMPS-LP. This revealed that the plume became trapped within a cyclonic  
730 circulation for several days across Eastern Russia and Alaska before travelling eastwards across North America and the North  
Atlantic. This agrees with other satellite observations used in previous studies (e.g., Kloss et al., 2021, Vaughan et al., 2020).  
When nudged to ERA5 reanalysis data the UKESM1 SO<sub>2</sub>only and SO<sub>2</sub>+ash simulations were able to represent the position  
of the main features of the plume evolution, including the cyclonic circulation. Similarly to other models (e.g. Haywood et al.,  
2010; de Leeuw et al., 2021) the model simulations produce a more diffuse SO<sub>2</sub> plume compared to observations due to a  
735 combination of model uncertainty and observational limits.

The distribution of the sulfate aerosol plume was examined using two satellite observations with comparisons to the UKESM1  
model simulations. The zonal evolution observed by CALIOP, and OMPS-LP followed a similar geographic evolution to the  
Sarychev Peak eruption in June 2009 (Haywood et al., 2010) which was to be expected since they are neighbouring volcanoes  
740 and the altitude and injection magnitude of Sarychev Peak (11 – 15km,  $1.2 \pm 0.2$  Tg) were similar to that of Raikoke (10 –  
15km,  $1.5 \pm 0.2$  Tg). Due to differences in minimum detection thresholds it was observed that the CALIOP data did not  
represent the long-term evolution of the sulfate aerosol plume well and similarly to other limb-instruments, OMPS-LP can fail  
to detect aerosol near the tropopause at the beginning of an eruption. Hence, we created a combined dataset consisting of both  
CALIOP and OMPS-LP aerosol extinction data. Data from the Mauna Loa Observatory provided additional corroborative  
745 evidence that the OMPS-LP observations were more appropriate after the plume had dispersed, with CALIOP observations  
showing no significant increase in sAOD for the eruption year. Model simulations differed in the MLO region, with the

SO<sub>2</sub>+ash case presenting similar values of sAOD to both the OMPS-LP and AERONET observations. In contrast, the SO<sub>2</sub>only simulation revealed values of sAOD much lower than those seen in the observations and SO<sub>2</sub>+ash case.

750 We then studied the observed Ångström Exponent utilising the OMPS-LP 869nm and 510nm wavelength aerosol extinction coefficient retrievals. Throughout the first 50 days after the eruption the AE was less than one, indicating the presence of large aerosol particles. Comparing the observations to both the SO<sub>2</sub>only and SO<sub>2</sub>+ash UKESM1 scenario demonstrates that whilst both models do not capture the observations completely, the SO<sub>2</sub>+ash scenario better represents the change in aerosol size after the eruption. It is also an indicator that the model removes the ash much faster than we see in the observations. Zhu et al.,  
755 2020 proposed that after the 2014 Mount Kelud eruption the volcanic aerosol layer was primarily composed of low density, super-micron sized ash. Most model simulations assume volcanic ash particles are denser than the pumice-like particles observed in Zhu et al. (2020) and hence the ash particles in model simulations fall out more quickly. Supplementary figure 2 highlights the relatively small and short impact the ash in the model has on the stratospheric aerosol optical depth itself. Instead we see in Figs. 9 and 10 how the ash produces a self-lofting effect onto the sulfate aerosol, extending the stratospheric lifetime  
760 of the aerosol. This could explain the difference between the observations and the SO<sub>2</sub>+ash model case. Obviously, there are limitations to our assumption that the ash is externally mixed with the sulfate aerosol as in reality there will be varying degrees of internal and external mixture.

It is possible that the observations were also influenced by the Canadian and Siberian wildfires which occurred in the summer  
765 of 2019. A few days before the Raikoke eruption (17<sup>th</sup> June 2019), wildfires in Alberta, Canada produced biomass burning aerosols and formed pyrocumulus clouds which entered the lower stratosphere. By late June the resulting aerosol layers arrived over the UK and Europe, this was only a few days before aerosols originating from the Raikoke plume were observed by UK lidars (Osborne et al., 2022). The Siberian wildfires were extreme and lasted from 19<sup>th</sup> July to 14<sup>th</sup> August 2019 (between 28-54 days after the eruption; Johnson et al., 2019) injecting wildfire smoke into the troposphere near to the Arctic region.  
770 Ohneiser et al., (2021) and Ansmann et al. (2021) suggested that the influence from the Siberian wildfire smoke increased the aerosol optical depth across the Arctic region. However, this finding is challenged by Boone et al., (2022). Whilst there might have been some influence on the aerosol optical properties and distribution from these events, our simulations suggest that the SO<sub>2</sub>+ash model provides a reasonable representation of the Raikoke eruption without including the Siberian wildfires in the model simulation. Our work certainly shows that using the results from a single climate model simulation of Sarychev to infer  
775 aerosol optical depths for other volcanic eruptions such as Raikoke is inadvisable. Further work appears necessary to elucidate whether biomass burning smoke aerosols play a role in the elevated aerosol concentrations in the polar vortex during the northern hemisphere winter of 2020.

We utilised the CALIOP aerosol extinction coefficient night-time retrievals to examine the evolution of the vertical profile of  
780 the plume. We initially observed two distinct peaks just above and just below the average tropopause height before a singular

785 peak at around 14km was observed from August onwards. The SO<sub>2</sub>+ash model represents the altitude of the aerosol well throughout the months following the eruption, however the SO<sub>2</sub>only simulation displayed values of aerosol extinction consistently lower in altitude (Figs. 9 and 10) resulting in a much faster decay rate due to transfer to the troposphere through tropospheric folds. The modelled aerosol extinction peak was prematurely early and overestimated in both scenarios which could be due to the rate of coagulation in the stratosphere or how the model represents new particle formation. After more moderate volcanic eruptions the rate of coagulation can be slower resulting in smaller less optically active particles and a delayed aerosol extinction peak. We see in both model simulations the accumulation mode dominates the column aerosol burden. This could suggest that the rate of transfer from optically inactive Aitken to optically active accumulation mode in the model may be too fast.

790

Finally the impact of the modelled Raikoke eruption was compared to the HadGEM2 simulation of the Sarychev Peak eruption. The Northern Hemisphere peak mean perturbation to the sAOD after the Sarychev Peak eruption was 0.01 compared to 0.03 after the Raikoke eruption. The greatest radiative forcing on the Northern Hemisphere after the Raikoke eruption was 0.48 Wm<sup>-2</sup>, almost double that seen in the July following the Sarychev Peak eruption, 0.24 Wm<sup>-2</sup>, despite only a 25% increase in the injected SO<sub>2</sub> amount. Whilst the eruptions were similar in altitude and latitude, the impact seen in UKESM1 is far greater in Raikoke than after Sarychev Peak. Some of these differences may stem from the large dependence on meteorology that has been noted for low-altitude eruptions (Jones et al., 2016), with differences in how the SO<sub>2</sub> was injected into the model contributing to this. We also compare an SO<sub>2</sub>only Raikoke-only simulation and find a Northern Hemispheric peak AOD of approximately 0.02 but a greater peak radiative forcing of 0.55 Wm<sup>-2</sup>. This is to be expected since the injected ash would contribute a positive radiative forcing counterbalancing the negative radiative forcing from the sulfate aerosol. Finally, UKESM1 represents a major advance from HadGEM2 with a new core physical model including a well-resolved stratosphere and enhanced tropospheric-stratospheric chemistry.

805 Accurately modelling the evolution of volcanic plumes and therefore identifying the impacts they have on the climate is a difficult task. Our analysis provides several lines of evidence to suggest that including ash in model emission schemes can improve the representation of volcanic plumes in global climate models. Whilst the model is not perfect at representing each process it provides reasonable *e*-folding times for the conversion of SO<sub>2</sub> to sulfate aerosol and models the geographic distribution of the aerosol well. Future work might consider internal mixture of sulfate and ash aerosol which could yield differences in the aerosol microphysical and optical properties. Including smoke aerosol in simulations of this eruption would also be useful to identify if this would improve the model performance. A better representation of volcanic ash could also be applied, since this study used mineral dust as a proxy since the refractive indices and size distributions are similar. Ultimately, this study has shown that volcanic emissions are far more complicated than simple injections of SO<sub>2</sub> and that limitations in remote sensing observations hamper definitive attribution of particle composition. These results suggest the strong need for in situ sampling of aerosol from instrumentation on airborne observational platforms. While such measurements of ash-sulfate



815 mixtures have been performed following eruptions that predominantly loaded the troposphere (e.g. Johnson et al., 2021; Turnbull et al., 2012; Newman et al., 2012), the dearth of such measurements in the stratosphere means that definitive attribution of aerosol composition, and microphysical and optical properties remains extremely challenging.

Final caveats to our modelling study include the fact that we do not include any emission of water vapor (e.g. Joshi and Jones, 820 2009) nor of any halogens (e.g. Staunton-Sykes et al., 2020); these species are commonly co-emitted with volcanic eruptions and may influence the oxidation rates of sulfur dioxide and the detailed evolution of the resultant aerosol plume.

### **Code and data availability**

825 The data is available at <https://doi.org/10.5281/zenodo.7602563> and the code to reproduce the figures is at  
830 <https://zenodo.org/badge/latestdoi/596982123>

### **Author Contributions**

AW, MO and LDP analysed the satellite and in-situ data and created the combined observational dataset. AJ and JH devised  
830 the experimental set up for UKESM1. AW, AJ and JH analysed the results of the simulations. AW prepared the manuscript  
with contributions from all co-authors.

### **Competing interests**

The authors declare that they have no conflict of interest.

### **835 Acknowledgements**

AW was funded via a UKRI Centre for Doctoral Training in Environmental Intelligence PhD studentship hosted by the  
University of Exeter. JH, AJ, MO was supported by the Met Office Hadley Centre Climate Programme funded by BEIS. JH  
would also like to acknowledge support from the NERC funded EXTEND project (NE/W003880/1) and from SilverLining  
through its Safe Climate Research Initiative. LDP was supported from the NERC funded SASSO standard grant (NE/  
840 S00212X/1). JH and DP would like to acknowledge the support of the NERC funded ADVANCE project (NE/T006897/1).

### **References**

- Abdelkader, M., Stenchikov, G., Pozzer, A., Tost, H., and Lelieveld, J.: The effect of ash, water vapor, and heterogeneous  
chemistry on the evolution of a Pinatubo-size volcanic cloud, *Atmos. Chem. Phys.*, 23, 471-500, 10.5194/acp-23-471-2023,  
2023.
- 845 Ansmann, A., Ohneiser, K., Mamouri, R. E., Knopf, D. A., Veselovskii, I., Baars, H., Engelmann, R., Foth, A., Jimenez, C.,  
Seifert, P., and Barja, B.: Tropospheric and stratospheric wildfire smoke profiling with lidar: mass, surface area, CCN, and  
INP retrieval, *Atmos. Chem. Phys.*, 21, 9779-9807, 10.5194/acp-21-9779-2021, 2021.
- 850 Archibald, A. T., O'Connor, F. M., Abraham, N. L., Archer-Nicholls, S., Chipperfield, M. P., Dalvi, M., Folberth, G. A.,  
Dennison, F., Dhomse, S. S., Griffiths, P. T., Hardacre, C., Hewitt, A. J., Hill, R. S., Johnson, C. E., Keeble, J., Köhler, M. O.,  
Morgenstern, O., Mulcahy, J. P., Ordóñez, C., Pope, R. J., Rumbold, S. T., Russo, M. R., Savage, N. H., Sellar, A., Stringer,  
M., Turnock, S. T., Wild, O., and Zeng, G.: Description and evaluation of the UKCA stratosphere–troposphere chemistry  
855 1223-2020, 2020.

Balkanski, Y., Schulz, M., Claquin, T., and Guibert, S.: Reevaluation of Mineral aerosol radiative forcings suggests a better agreement with satellite and AERONET data, *Atmos. Chem. Phys.*, 7, 81-95, 10.5194/acp-7-81-2007, 2007.

860 Barnes, J. E. and Hofmann, D. J.: Lidar measurements of stratospheric aerosol over Mauna Loa Observatory, *Geophysical Research Letters*, 24, 1923-1926, 10.1029/97gl01943, 1997.

Bednarz, E. M., Visioni, D., Kravitz, B., Jones, A., Haywood, J. M., Richter, J., MacMartin, D. G., and Braesicke, P.: Climate response to off-equatorial stratospheric sulfur injections in three Earth system models – Part 2: Stratospheric and free-tropospheric response, *Atmos. Chem. Phys.*, 23, 687-709, 10.5194/acp-23-687-2023, 2023.

Bellouin, N., Rae, J., Jones, A., Johnson, C., Haywood, J., and Boucher, O.: Aerosol forcing in the Climate Model Intercomparison Project (CMIP5) simulations by HadGEM2-ES and the role of ammonium nitrate, *Journal of Geophysical Research: Atmospheres*, 116, <https://doi.org/10.1029/2011JD016074>, 2011.

870

Bluth, G. J. S., Doiron, S. D., Schnetzler, C. C., Krueger, A. J., and Walter, L. S.: Global Tracking of the SO<sub>2</sub> Clouds from the June 1991 Mount Pinatubo Eruptions, *Geophysical Research Letters*, 19, 151-154, 1992.

Boone, C. D., Bernath, P. F., Labelle, K., and Crouse, J.: Stratospheric Aerosol Composition Observed by the Atmospheric Chemistry Experiment Following the 2019 Raikoke Eruption, *Journal of Geophysical Research: Atmospheres*, 127, e2022JD036600, <https://doi.org/10.1029/2022JD036600>, 2022.

Bruckert, J., Hoshyaripour, G. A., Horváth, Á., Muser, L. O., Prata, F. J., Hoose, C., and Vogel, B.: Online treatment of eruption dynamics improves the volcanic ash and SO<sub>2</sub> dispersion forecast: case of the 2019 Raikoke eruption, *Atmospheric Chemistry and Physics*, 22, 3535-3552, 10.5194/acp-22-3535-2022, 2022.

880

Cai, Z., Griessbach, S., and Hoffmann, L.: Improved estimation of volcanic SO<sub>2</sub> injections from satellite retrievals and Lagrangian transport simulations: the 2019 Raikoke eruption, *Atmos. Chem. Phys.*, 22, 6787-6809, 10.5194/acp-22-6787-2022, 2022.

885

Campbell, J. R., Tackett, J. L., Reid, J. S., Zhang, J., Curtis, C. A., Hyer, E. J., Sessions, W. R., Westphal, D. L., Prospero, J. M., Welton, E. J., Omar, A. H., Vaughan, M. A., and Winker, D. M.: Evaluating nighttime CALIOP 0.532 μm aerosol optical depth and extinction coefficient retrievals, *Atmos. Meas. Tech.*, 5, 2143-2160, 10.5194/amt-5-2143-2012, 2012.

- 890 Casati, B., Wilson, L. J., Stephenson, D. B., Nurmi, P., Ghelli, A., Pocernich, M., Damrath, U., Ebert, E. E., Brown, B. G., and  
Mason, S.: Forecast verification: current status and future directions, *Meteorological Applications*, 15, 3-18,  
<https://doi.org/10.1002/met.52>, 2008.
- Chouza, F., Leblanc, T., Barnes, J., Brewer, M., Wang, P., and Koon, D.: Long-term (1999–2019) variability of stratospheric  
895 aerosol over Mauna Loa, Hawaii, as seen by two co-located lidars and satellite measurements, *Atmos. Chem. Phys.*, 20, 6821-  
6839, [10.5194/acp-20-6821-2020](https://doi.org/10.5194/acp-20-6821-2020), 2020.
- Christian, K., Wang, J., Ge, C., Peterson, D., Hyer, E., Yorks, J., and McGill, M.: Radiative Forcing and Stratospheric Warming  
of Pyrocumulonimbus Smoke Aerosols: First Modeling Results With Multisensor (EPIC, CALIPSO, and CATS) Views from  
900 Space, *Geophysical Research Letters*, 46, 10061-10071, <https://doi.org/10.1029/2019GL082360>, 2019.
- Clarisse, L., Hurtmans, D., Clerbaux, C., Hadji-Lazaro, J., Ngadi, Y., and Coheur, P. F.: Retrieval of sulphur dioxide from the  
infrared atmospheric sounding interferometer (IASI), *Atmospheric Measurement Techniques*, 5, 581-594, [10.5194/amt-5-581-  
2012](https://doi.org/10.5194/amt-5-581-2012), 2012.
- 905 Corradini, S., Merucci, L., Prata, A. J., and Piscini, A.: Volcanic ash and SO<sub>2</sub> in the 2008 Kasatochi eruption: Retrievals  
comparison from different IR satellite sensors, *Journal of Geophysical Research: Atmospheres*, 115,  
<https://doi.org/10.1029/2009JD013634>, 2010.
- 910 Damany-Pearce, L., Johnson, B., Wells, A., Osborne, M., Allan, J., Belcher, C., Jones, A., and Haywood, J.: Australian  
wildfires cause the largest stratospheric warming since Pinatubo and extends the lifetime of the Antarctic ozone hole, *Scientific  
Reports*, 12, 12665, 2022.
- de Leeuw, J., Schmidt, A., Witham, C. S., Theys, N., Taylor, I. A., Grainger, R. G., Pope, R. J., Haywood, J., Osborne, M.,  
915 and Kristiansen, N. I.: The 2019 Raikoke volcanic eruption – Part 1: Dispersion model simulations and satellite retrievals of  
volcanic sulfur dioxide, *Atmospheric Chemistry and Physics*, 21, 10851-10879, [10.5194/acp-21-10851-2021](https://doi.org/10.5194/acp-21-10851-2021), 2021.
- Dhomse, S. S., Emmerson, K. M., Mann, G. W., Bellouin, N., Carslaw, K. S., Chipperfield, M. P., Hommel, R., Abraham, N.  
L., Telford, P., Braesicke, P., Dalvi, M., Johnson, C. E., O'Connor, F., Morgenstern, O., Pyle, J. A., Deshler, T., Zawodny, J.  
920 M., and Thomason, L. W.: Aerosol microphysics simulations of the Mt.~Pinatubo eruption with the UM-UKCA composition-  
climate model, *Atmospheric Chemistry and Physics*, 14, 11221-11246, [10.5194/acp-14-11221-2014](https://doi.org/10.5194/acp-14-11221-2014), 2014.

Edwards, J. and Slingo, A.: Studies with a flexible new radiation code. I: Choosing a configuration for a large-scale model, *Quarterly Journal of the Royal Meteorological Society*, 122, 689-719, 1996.

925

Fromm, M., Bevilacqua, R., Servranckx, R., Rosen, J., Thayer, J. P., Herman, J., and Larko, D.: Pyro-cumulonimbus injection of smoke to the stratosphere: Observations and impact of a super blowup in northwestern Canada on 3–4 August 1998, *Journal of Geophysical Research: Atmospheres*, 110, <https://doi.org/10.1029/2004JD005350>, 2005.

930 Fromm, M., Kablick, G., Nedoluha, G., Carboni, E., Grainger, R., Campbell, J., and Lewis, J.: Correcting the record of volcanic stratospheric aerosol impact: Nabro and Sarychev Peak, *Journal of Geophysical Research: Atmospheres*, 119, 10,343-310,364, [10.1002/2014jd021507](https://doi.org/10.1002/2014jd021507), 2014.

Gordeev, E. I. and Girina, O. A.: Volcanoes and their hazard to aviation, *Herald of the Russian Academy of Sciences*, 84, 1-8, [10.1134/s1019331614010079](https://doi.org/10.1134/s1019331614010079), 2014.

935

Gorkavyi, N., Krotkov, N., Li, C., Lait, L., Colarco, P., Carn, S., DeLand, M., Newman, P., Schoeberl, M., Taha, G., Torres, O., Vasilkov, A., and Joiner, J.: Tracking aerosols and SO<sub>2</sub> clouds from the Raikoke eruption: 3D view from satellite observations, *Atmospheric Measurement Techniques*, 14, 7545-7563, [10.5194/amt-14-7545-2021](https://doi.org/10.5194/amt-14-7545-2021), 2021.

940

Guo, S., Bluth, G. J. S., Rose, W. I., Watson, I. M., and Prata, A. J.: Re-evaluation of SO<sub>2</sub> release of the 15 June 1991 Pinatubo eruption using ultraviolet and infrared satellite sensors, *Geochemistry, Geophysics, Geosystems*, 5, n/a-n/a, [10.1029/2003gc000654](https://doi.org/10.1029/2003gc000654), 2004.

Haynes, P.: STRATOSPHERIC DYNAMICS, *Annual Review of Fluid Mechanics*, 37, 263-293, [10.1146/annurev.fluid.37.061903.175710](https://doi.org/10.1146/annurev.fluid.37.061903.175710), 2005.

945

Haywood, J. M., Jones, A., Clarisse, L., Bourassa, A., Barnes, J., Telford, P., Bellouin, N., Boucher, O., Agnew, P., Clerbaux, C., Coheur, P., Degenstein, D., and Braesicke, P.: Observations of the eruption of the Sarychev volcano and simulations using the HadGEM2 climate model, *Journal of Geophysical Research*, 115, [10.1029/2010jd014447](https://doi.org/10.1029/2010jd014447), 2010.

950

Haywood, J. M., Jones, A., and Jones, G. S.: The impact of volcanic eruptions in the period 2000-2013 on global mean temperature trends evaluated in the HadGEM2-ES climate model, *Atmospheric Science Letters*, 15, 92-96, [10.1002/asl2.471](https://doi.org/10.1002/asl2.471), 2014.

955 Haywood, J. M., Roberts, D. L., Slingo, A., Edwards, J. M., and Shine, K. P.: General Circulation Model Calculations of the Direct Radiative Forcing by Anthropogenic Sulfate and Fossil-Fuel Soot Aerosol, *Journal of Climate*, 10, 1562-1577, 10.1175/1520-0442(1997)010<1562:Gcmcot>2.0.Co;2, 1997.

Haywood, J. M. and Shine, K. P.: The effect of anthropogenic sulfate and soot aerosol on the clear sky planetary radiation  
960 budget, *Geophysical Research Letters*, 22, 603-606, <https://doi.org/10.1029/95GL00075>, 1995.

Hedelt, P., Efremenko, D. S., Loyola, D. G., Spurr, R., and Clarisse, L.: Sulfur dioxide layer height retrieval from Sentinel-5 Precursor/TROPOMI using FP\_ILM, *Atmospheric Measurement Techniques*, 12, 5503-5517, 10.5194/amt-12-5503-2019, 2019.

965

Hirsch, E. and Koren, I.: Record-breaking aerosol levels explained by smoke injection into the stratosphere, *Science*, 371, 1269-1274, 2021.

Holben, B. N., Eck, T. F., Slutsker, I. a., Tanre, D., Buis, J., Setzer, A., Vermote, E., Reagan, J. A., Kaufman, Y., and Nakajima,  
970 T.: AERONET—A federated instrument network and data archive for aerosol characterization, *Remote sensing of environment*, 66, 1-16, 1998.

Jégou, F., Berthet, G., Brogniez, C., Renard, J. B., François, P., Haywood, J. M., Jones, A., Bourgeois, Q., Lurton, T., Auriol, F., Godin-Beekmann, S., Guimbaud, C., Krysztofiak, G., Gaubicher, B., Chartier, M., Clarisse, L., Clerbaux, C., Balois, J. Y.,  
975 Verwaerde, C., and Dauteron, D.: Stratospheric aerosols from the Sarychev volcano eruption in the 2009 Arctic summer, *Atmos. Chem. Phys.*, 13, 6533-6552, 10.5194/acp-13-6533-2013, 2013.

Johnson, B., Turnbull, K., Brown, P., Burgess, R., Dorsey, J., Baran, A. J., Webster, H., Haywood, J., Cotton, R., Ulanowski, Z., Hesse, E., Woolley, A., and Rosenberg, P.: In situ observations of volcanic ash clouds from the FAAM aircraft during the  
980 eruption of Eyjafjallajökull in 2010, *Journal of Geophysical Research: Atmospheres*, 117, 10.1029/2011jd016760, 2012.

Johnson, B., Turnbull, K., Brown, P., Burgess, R., Dorsey, J., Baran, A. J., Webster, H., Haywood, J., Cotton, R., Ulanowski, Z., Hesse, E., Woolley, A., and Rosenberg, P.: In situ observations of volcanic ash clouds from the FAAM aircraft during the eruption of Eyjafjallajökull in 2010, *Journal of Geophysical Research: Atmospheres*, 117,  
985 <https://doi.org/10.1029/2011JD016760>, 2012.

Johnson, J., Taha, G., Loughman, R., Zhu, T., and DeLand, M.: README Document for the Suomi-NPP OMPS LP L2 AER Daily Product, 2020.

- 990 Johnson, M. S., Strawbridge, K., Knowland, K. E., Keller, C., and Travis, M.: Long-range transport of Siberian biomass  
burning emissions to North America during FIREX-AQ, *Atmospheric Environment*, 252, 10.1016/j.atmosenv.2021.118241,  
2021.
- Jones, A. C., Haywood, J. M., Dunstone, N., Emanuel, K., Hawcroft, M. K., Hodges, K. I., and Jones, A.: Impacts of  
995 hemispheric solar geoengineering on tropical cyclone frequency, *Nat Commun*, 8, 1382, 10.1038/s41467-017-01606-0, 2017.
- Jones, A. C., Haywood, J. M., Jones, A., and Aquila, V.: Sensitivity of volcanic aerosol dispersion to meteorological  
conditions: A Pinatubo case study, *Journal of Geophysical Research: Atmospheres*, 121, 6892-6908,  
<https://doi.org/10.1002/2016JD025001>, 2016.
- 1000
- Joshi, M. M. and Jones, G. S.: The climatic effects of the direct injection of water vapour into the stratosphere by large volcanic  
eruptions, *Atmos. Chem. Phys.*, 9, 6109-6118, 10.5194/acp-9-6109-2009, 2009.
- Karagulian, F., Clarisse, L., Clerbaux, C., Prata, A. J., Hurtmans, D., and Coheur, P. F.: Detection of volcanic SO<sub>2</sub>, ash, and  
1005 H<sub>2</sub>SO<sub>4</sub> using the Infrared Atmospheric Sounding Interferometer (IASI), *Journal of Geophysical Research*, 115,  
10.1029/2009jd012786, 2010.
- Kloss, C., Berthet, G., Sellitto, P., Ploeger, F., Taha, G., Tidiga, M., Eremenko, M., Bossolasco, A., Jégou, F., Renard, J.-B.,  
and Legras, B.: Stratospheric aerosol layer perturbation caused by the 2019 Raikoke and Ulawun eruptions and their radiative  
1010 forcing, *Atmospheric Chemistry and Physics*, 21, 535-560, 10.5194/acp-21-535-2021, 2021.
- Kravitz, B., Robock, A., and Bourassa, A.: Negligible climatic effects from the 2008 Okmok and Kasatochi volcanic eruptions,  
*Journal of Geophysical Research*, 115, 10.1029/2009jd013525, 2010.
- 1015 Langmann, B.: On the Role of Climate Forcing by Volcanic Sulphate and Volcanic Ash, *Advances in Meteorology*, 2014, 1-  
17, 10.1155/2014/340123, 2014.
- Lawrence, M. G., Schäfer, S., Muri, H., Scott, V., Oschlies, A., Vaughan, N. E., Boucher, O., Schmidt, H., Haywood, J., and  
Scheffran, J.: Evaluating climate geoengineering proposals in the context of the Paris Agreement temperature goals, *Nature*  
1020 *communications*, 9, 1-19, 2018.

- Lee, K. H., Li, Z., Kim, Y. J., and Kokhanovsky, A.: Atmospheric Aerosol Monitoring from Satellite Observations: A History of Three Decades, in: Atmospheric and Biological Environmental Monitoring, edited by: Kim, Y. J., Platt, U., Gu, M. B., and Iwahashi, H., Springer Netherlands, Dordrecht, 13-38, 10.1007/978-1-4020-9674-7\_2, 2009.
- 1025
- Mann, G., Carslaw, K., Ridley, D., Spracklen, D., Pringle, K., Merikanto, J., Korhonen, H., Schwarz, J., Lee, L., and Manktelow, P.: Intercomparison of modal and sectional aerosol microphysics representations within the same 3-D global chemical transport model, *Atmospheric Chemistry and Physics*, 12, 4449-4476, 2012.
- 1030
- Mann, G. W., Carslaw, K. S., Spracklen, D. V., Ridley, D. A., Manktelow, P. T., Chipperfield, M. P., Pickering, S. J., and Johnson, C. E.: Description and evaluation of GLOMAP-mode: a modal global aerosol microphysics model for the UKCA composition-climate model, *Geoscientific Model Development*, 3, 519-551, 10.5194/gmd-3-519-2010, 2010.
- McCormick, P. M., Thomason, L., and Trepte, C.: Atmospheric effects of the Mt Pinatubo eruption, *Nature*, 373, 1995.
- 1035
- Millington, S. C., Saunders, R. W., Francis, P. N., and Webster, H. N.: Simulated volcanic ash imagery: A method to compare NAME ash concentration forecasts with SEVIRI imagery for the Eyjafjallajökull eruption in 2010, *Journal of Geophysical Research: Atmospheres*, 117, <https://doi.org/10.1029/2011JD016770>, 2012.
- 1040
- Muser, L. O., Hoshyaripour, G. A., Bruckert, J., Horváth, Á., Malinina, E., Wallis, S., Prata, F. J., Rozanov, A., von Savigny, C., Vogel, H., and Vogel, B.: Particle aging and aerosol–radiation interaction affect volcanic plume dispersion: evidence from the Raikoke 2019 eruption, *Atmospheric Chemistry and Physics*, 20, 15015-15036, 10.5194/acp-20-15015-2020, 2020.
- Newman, S. M., Clarisse, L., Hurtmans, D., Marenco, F., Johnson, B., Turnbull, K., Havemann, S., Baran, A. J., O'Sullivan, D., and Haywood, J.: A case study of observations of volcanic ash from the Eyjafjallajökull eruption: 2. Airborne and satellite radiative measurements, *Journal of Geophysical Research: Atmospheres*, 117, <https://doi.org/10.1029/2011JD016780>, 2012.
- 1045
- Niemeier, U., Riede, F., and Timmreck, C.: Simulation of ash clouds after a Laacher See-type eruption, *Clim. Past*, 17, 633-652, 10.5194/cp-17-633-2021, 2021.
- 1050
- Niemeier, U., Timmreck, C., Graf, H.-F., Kinne, S., Rast, S., and S., S.: Initial fate of fine ash and sulfur from large volcanic eruptions, *Atmospheric Chemistry and Physics*, 2009.
- Ohneiser, K., Ansmann, A., Chudnovsky, A., Engelmann, R., Ritter, C., Veselovskii, I., Baars, H., Gebauer, H., Griesche, H., 1055 Radenz, M., Hofer, J., Althausen, D., Dahlke, S., and Maturilli, M.: The unexpected smoke layer in the High Arctic winter



- stratosphere during MOSAiC 2019–2020, *Atmospheric Chemistry and Physics*, 21, 15783-15808, 10.5194/acp-21-15783-2021, 2021.
- Osborne, M. J., de Leeuw, J., Witham, C., Schmidt, A., Beckett, F., Kristiansen, N., Buxmann, J., Saint, C., Welton, E. J.,  
1060 Fochesatto, J., Gomes, A. R., Bundke, U., Petzold, A., Marenco, F., and Haywood, J.: The 2019 Raikoke volcanic eruption –  
Part 2: Particle-phase dispersion and concurrent wildfire smoke emissions, *Atmospheric Chemistry and Physics*, 22, 2975-  
2997, 10.5194/acp-22-2975-2022, 2022.
- Peterson, D. A., Campbell, J. R., Hyer, E. J., Fromm, M. D., Kablick, G. P., Cossuth, J. H., and DeLand, M. T.: Wildfire-  
1065 driven thunderstorms cause a volcano-like stratospheric injection of smoke, *npj Climate and Atmospheric Science*, 1, 30,  
10.1038/s41612-018-0039-3, 2018.
- Plumb, R. A.: A “tropical pipe” model of stratospheric transport, *Journal of Geophysical Research: Atmospheres*, 101, 3957-  
3972, <https://doi.org/10.1029/95JD03002>, 1996.
- 1070 Ridley, J. K., Blockley, E. W., Keen, A. B., Rae, J. G. L., West, A. E., and Schroeder, D.: The sea ice model component of  
HadGEM3-GC3.1, *Geoscientific Model Development*, 11, 713-723, 10.5194/gmd-11-713-2018, 2018.
- Robock, A.: Volcanic eruptions and climate, *Reviews of Geophysics*, 38, 191-219, 10.1029/1998rg000054, 2000.
- 1075 Sellar, A. A., Jones, C. G., Mulcahy, J. P., Tang, Y., Yool, A., Wiltshire, A., O'Connor, F. M., Stringer, M., Hill, R., Palmieri,  
J., Woodward, S., Mora, L., Kuhlbrodt, T., Rumbold, S. T., Kelley, D. I., Ellis, R., Johnson, C. E., Walton, J., Abraham, N.  
L., Andrews, M. B., Andrews, T., Archibald, A. T., Berthou, S., Burke, E., Blockley, E., Carslaw, K., Dalvi, M., Edwards, J.,  
Folberth, G. A., Gedney, N., Griffiths, P. T., Harper, A. B., Hendry, M. A., Hewitt, A. J., Johnson, B., Jones, A., Jones, C. D.,  
1080 Keeble, J., Liddicoat, S., Morgenstern, O., Parker, R. J., Predoi, V., Robertson, E., Siahhaan, A., Smith, R. S., Swaminathan,  
R., Woodhouse, M. T., Zeng, G., and Zerroukat, M.: UKESM1: Description and Evaluation of the U.K. Earth System Model,  
*Journal of Advances in Modeling Earth Systems*, 11, 4513-4558, 10.1029/2019ms001739, 2019.
- Shallcross, S.: The role of volcanic ash in the global dispersion of the aerosol cloud from major tropical eruptions, University  
1085 of Leeds, 2020.
- Shallcross, S., Mann, G., Schmidt, A., Haywood, J., Beckett, F., Jones, A., Neely, R., Vaughan, G., and Dhomse, S.: Long-  
lived ultra-fine ash particles within the Pinatubo volcanic aerosol cloud and their potential impact on its global dispersion and  
radiative forcings, April 01, 2021, 10.5194/egusphere-egu21-16034, 2021.

1090

Staunton-Sykes, J., Aubry, T. J., Shin, Y. M., Weber, J., Marshall, L. R., Luke Abraham, N., Archibald, A., and Schmidt, A.: Co-emission of volcanic sulfur and halogens amplifies volcanic effective radiative forcing, *Atmos. Chem. Phys.*, 21, 9009-9029, 10.5194/acp-21-9009-2021, 2021.

1095 Stenchikov, G., Ukhov, A., Osipov, S., Ahmadov, R., Grell, G., Cady-Pereira, K., Mlawer, E., and Iacono, M.: How Does a Pinatubo-Size Volcanic Cloud Reach the Middle Stratosphere?, *Journal of Geophysical Research: Atmospheres*, 126, e2020JD033829, <https://doi.org/10.1029/2020JD033829>, 2021.

Storkey, D., Blaker, A. T., Mathiot, P., Megann, A., Aksenov, Y., Blockley, E. W., Calvert, D., Graham, T., Hewitt, H. T.,  
1100 Hyder, P., Kuhlbrodt, T., Rae, J. G. L., and Sinha, B.: UK Global Ocean GO6 and GO7: a traceable hierarchy of model resolutions, *Geoscientific Model Development*, 11, 3187-3213, 10.5194/gmd-11-3187-2018, 2018.

Taha, G.: OMPS-NPP L2 LP Aerosol Extinction Vertical Profile swath daily 3slit V2, Goddard Earth Sciences Data and Information Services Center (GES DISC) [dataset], 10.5067/CX2B9NW6FI27, 2020.

1105

Taha, G., Loughman, R., Zhu, T., Thomason, L., Kar, J., Rieger, L., and Bourassa, A.: OMPS LP Version 2.0 multi-wavelength aerosol extinction coefficient retrieval algorithm, *Atmospheric Measurement Techniques*, 14, 1015-1036, 10.5194/amt-14-1015-2021, 2021.

1110 Thomason, L.: Observations of a New SAGE II Aerosol Extinction Mode Following the Eruption of Mount Pinatubo, *Geophysical Research Letters*, 19, 1992.

Thomason, L. and Peter, T.: SPARC Assessment of Stratospheric Aerosol Properties (ASAP), 2006.

1115 Toledano, C., González, R., Fuertes, D., Cuevas, E., Eck, T. F., Kazadzis, S., Kouremeti, N., Gröbner, J., Goloub, P., Blarel, L., Román, R., Barreto, Á., Berjón, A., Holben, B. N., and Cachorro, V. E.: Assessment of Sun photometer Langley calibration at the high-elevation sites Mauna Loa and Izaña, *Atmos. Chem. Phys.*, 18, 14555-14567, 10.5194/acp-18-14555-2018, 2018.

1120 Toth, T. D., Campbell, J. R., Reid, J. S., Tackett, J. L., Vaughan, M. A., Zhang, J., and Marquis, J. W.: Minimum aerosol layer detection sensitivities and their subsequent impacts on aerosol optical thickness retrievals in CALIPSO level 2 data products, *Atmos Meas Tech*, 11, 499-514, 10.5194/amt-11-499-2018, 2018.

- 1125 Turnbull, K., Johnson, B., Marenco, F., Haywood, J., Minikin, A., Weinzierl, B., Schlager, H., Schumann, U., Leadbetter, S.,  
and Woolley, A.: A case study of observations of volcanic ash from the Eyjafjallajökull eruption: 1. In situ airborne  
observations, *Journal of Geophysical Research: Atmospheres*, 117, 2012.
- 1130 Turnbull, K., Johnson, B., Marenco, F., Haywood, J., Minikin, A., Weinzierl, B., Schlager, H., Schumann, U., Leadbetter, S.,  
and Woolley, A.: A case study of observations of volcanic ash from the Eyjafjallajökull eruption: 1. In situ airborne  
observations, *Journal of Geophysical Research: Atmospheres*, 117, <https://doi.org/10.1029/2011JD016688>, 2012.
- Vaughan, G., Wareing, D., and Ricketts, H.: Measurement Report: Lidar measurements of stratospheric aerosol following the  
2019 Raikoke and Ulawun volcanic eruptions, *Atmospheric Chemistry and Physics*, 21, 5597-5604, [10.5194/acp-21-5597-](https://doi.org/10.5194/acp-21-5597-2021)  
2021, 2021.
- 1135 Vernier, J. P., Fairlie, T. D., Deshler, T., Natarajan, M., Knepp, T., Foster, K., Wienhold, F. G., Bedka, K. M., Thomason, L.,  
and Trepte, C.: In situ and space-based observations of the Kelud volcanic plume: The persistence of ash in the lower  
stratosphere, *J Geophys Res Atmos*, 121, 11104-11118, [10.1002/2016JD025344](https://doi.org/10.1002/2016JD025344), 2016.
- 1140 Vioni, D., Bednarz, E. M., Lee, W. R., Kravitz, B., Jones, A., Haywood, J. M., and MacMartin, D. G.: Climate response to  
off-equatorial stratospheric sulfur injections in three Earth system models – Part 1: Experimental protocols and surface  
changes, *Atmos. Chem. Phys.*, 23, 663-685, [10.5194/acp-23-663-2023](https://doi.org/10.5194/acp-23-663-2023), 2023.
- 1145 Winker, D. M., Powell, K. A., Hu, Y., Omar, A., Vaughan, M. A., Liu, Z., Hunt, W. H., and Young, S. A.: Overview of the  
CALIPSO Mission and CALIOP Data Processing Algorithms, *Journal of Atmospheric and Oceanic Technology*, 26, 2310-  
2323, [10.1175/2009jtecha1281.1](https://doi.org/10.1175/2009jtecha1281.1), 2009.
- Woodward, S.: Modeling the atmospheric life cycle and radiative impact of mineral dust in the Hadley Centre climate model,  
*Journal of Geophysical Research: Atmospheres*, 106, 18155-18166, [10.1029/2000jd900795](https://doi.org/10.1029/2000jd900795), 2001.
- 1150 Woodward, S.: Hadley Centre Technical Note 87 Mineral Dust in HadGEM 2 March 2011,  
Woodward, S., Sellar, A., Tang, Y., Stringer, M., Yool, A., Robertson, E., and Wiltshire, A.: The simulation of mineral dust  
in the United Kingdom Earth System Model UKESM1., [10.5194/acp-2022-228](https://doi.org/10.5194/acp-2022-228), 2022.
- 1155 Yang, K.: OMPS-NPP L2 NM Sulfur Dioxide (SO<sub>2</sub>) Total and Tropospheric Column swath orbital V2 [dataset],  
[10.5067/A9O02ZH0J94R](https://doi.org/10.5067/A9O02ZH0J94R), 2017.

Yool, A., Popova, E. E., and Anderson, T. R.: MEDUSA-2.0: an intermediate complexity biogeochemical model of the marine carbon cycle for climate change and ocean acidification studies, *Geoscientific Model Development*, 6, 1767-1811, 1160 10.5194/gmd-6-1767-2013, 2013.

Zhu, Y., Toon, O. B., Jensen, E. J., Bardeen, C. G., Mills, M. J., Tolbert, M. A., Yu, P., and Woods, S.: Persisting volcanic ash particles impact stratospheric SO<sub>2</sub> lifetime and aerosol optical properties, *Nat Commun*, 11, 4526, 10.1038/s41467-020-18352-5, 2020.

1165